Laser cladding of bioactive glass coating on pure titanium substrate with highly refined grain structure

Szymon Bajda[1,*], Yijun Liu[2], Riccardo Tosi[2], Katarzyna Cholewa-Kowalska[3], Michal Krzyzanowski[1,4], Michal Dziadek[3,5], Mateusz Kopyscianski[1], Stanislaw Dymek[1], Alexander V. Polyakov[6], Irina P. Semenova[6] and Tomasz Tokarski[7]

[1] Faculty of Metals Engineering and Industrial Computer Science, AGH University of Science and Technology, Mickiewicza 30, Krakow 30-059, Poland
[2] Manufacturing Technology Centre, Ansty Park, Coventry, CV7 9JU, United Kingdom
[3] Faculty of Materials Science and Ceramics, AGH University of Science and Technology, Mickiewicza 30, Krakow 30-059, Poland
[4] Birmingham City University, Faculty Computing, Engineering & the Built Environment, Millenium Point, Curzon Street, Birmingham B4 7XG, United Kingdom
[5] Faculty of Chemistry, Jagiellonian University, Golebia 24, Krakow 31-007, Poland
[6] Institute of Physics of Advanced Materials, Ufa State Aviation Technical University, 12 K. Marx Str., Ufa 450008, Russia
[7] Academic Center of Materials and Nanotechnology, AGH University of Science and Technology, Mickiewicza 30, Krakow 30-059, Poland

* Corresponding author: Szymon Bajda, e-mail: sbajda@agh.edu.pl

Keywords: laser cladding, ultrafine-grained structure, pure titanium, bioactive glass, numerical analysis, in vitro

Abstract

Free from toxic elements biomaterial potentially applicable for load bearing biomedical implants was obtained for the first time by laser cladding of S520 bioactive glass onto ultrafine-grained commercially pure titanium. The cladding process affected the refined structure of the substrate inducing martensitic transformation near its surface. The α' acicular martensite gradually passes into relatively large grains with increasing distance from the substrate surface, which subsequently are transformed into smaller grains of about 2 μm in diameter. Both the melted zone, where the martensite crystalline structure was found, and the HAZ are characterized by relatively lower hardness in comparison with that of the substrate core indicating increased ductility. Such a combination of zones with different properties may have a synergistic effect and is beneficial for the obtained biomaterial. A characteristic region in the form of about 3 μm width band was formed in the melted zone at about 10 μm below the titanium surface. The results of EDS analysis indicate that several glass elements moved into the region while the titanium content in the same area was decreased. High bioactivity of the coated S520 glass was revealed by in vitro testing with SBF solution and almost complete reduction of P concentration occurred after 14 days.

1. Introduction

Biomaterials can be used in regenerative medicine to replace or enhance lost and damaged parts of the human body. Such materials include metals, ceramics, polymers, and composites. The mandatory feature for biomaterials is their biocompatibility, which is an ability of a material to perform its desired function without causing any local or systemic adverse response

in the human organism [1]. Based on biocompatibility and according to their reaction with body tissue, biomaterials can be classified into bioinert, bioactive and bioresorbable materials [2].

Bioinert materials do not initiate a response or interact being placed in the human body. These include titanium and its alloys, stainless steel and cobalt-chromium alloys [3,4]. Once placed in the human body, bioinert implants have minimal interaction with the neighbouring tissue and do not form chemical or biological bonds at the tissue/implant interface that may result in relative movements at the interface accelerating wear of their surfaces and stimulating inflammatory responses [5]. Potential application of such implants can be effective only when the prosthesis is implanted with a strong mechanical fit and loaded with compression. With this in mind, certain fixation methods have been developed, such as cementation, to achieve adhesion between a bioinert material and the attached bone [6]. Another approach is using natural adhesive phenomena to generate morphological (mechanical interlock) and biological fixation (tissue ingrowth into porous implant) [7,8]. In both cases it appears that the adhesion problem still exists motivating the search for alternative fixation methods.

Bioactive materials are defined as materials that stimulate a beneficial body's response at the interface, particularly bonding to a host tissue [9]. Bioactive materials attracted the attention of the whole world in the early 70s, when Professor Larry Hench discovered a special glass, called Bioglass®, with its ability to bond with attached bone [10]. The idea behind the invention was creating a material that, after implantation in human body, could form a hydroxyapatite (HA) layer on its surface that could establish a living bond with the host [11]. Indeed, the formation of HA has been confirmed by numerous studies both in vivo and in vitro [12,13]. This bonding mechanism has been termed "bioactive fixation" [14]. Its main advantage is that the bioactive connection with the bone may reach strength even greater than strength of the bone after 3-6 months [8].

Bioresorbable materials are able to be degraded in a physiological environment into products that are either metabolized into non-toxic degradation products or biologically absorbed, being replaced by the natural tissue [15]. Their degradation rate should be consistent with the rate of natural tissue formation. Moreover, bioresorbable implants should be able to provide adequate mechanical support during the replacement process to match the healing time [16].

Bioactive glasses are one of the most important bioactive and bioresorbable materials. They are solid and hard materials consisting of the main component SiO_2 and several additional basic components, which usually are Na_2O, CaO, MgO, P_2O_5 and K_2O. By varying any of them, different types of bioactive glasses can be made [17]. Their high bioactivity, osteoconduction and osteostimulation allows them to be used as small bone implants, bone filling materials and to be used in dental applications [18]. Bioactive glasses are attractive bioactive and bioresorbable materials. However, their poor mechanical properties and brittleness limit their clinical applications to non-load bearing implants [19]. They can also be applied as coatings on a mechanically tough bioinert substrate to enhance the fixation and osteointegration of the entire implant, in which the metallic substrate reduces the risk of its early failure [2]. Coating a metallic component with bioactive glass layer has three main objectives:

1) to provide the bioactivity allowing the implant to bond with host tissue,
2) to protect the metallic substrate from corrosion,
3) to protect the tissues from corrosion products which could induce adverse reaction in human organism [20].

The mentioned above mechanically tough bioinert substrates can be made of commercially available titanium alloys, such as Ti-6Al-4V, which are commonly used nowadays as materials for load bearing medical implants due to their exceptional mechanical properties and biocompatibility [21]. However, it has been reported that the presence of alloying elements, such as aluminium and vanadium, may be potentially toxic when released into human

system [22,23]. This issue may be resolved by replacing titanium alloys with commercially pure titanium (cpTi) having highly refined grain structure free of potentially toxic elements [24]. The yield and ultimate strength of ultrafine-grained cpTi can exceed 1000 MPa, which is even higher than those of conventional titanium alloys [22,25]. Moreover, it was proven that osseointegration [22] and proliferation behaviour [26] are better for ultrafine-grained cpTi than that of a conventional cpTi. Such bulk refined structures can be obtained using severe plastic deformation (SPD) processing [27,28]. We found only one publication concerning bioactive coatings on ultrafine-grained cpTi, where radiofrequency magnetron sputtering was used for deposition of thin bioactive Zn substituted HA coating onto ultrafine-grained cpTi [29]. However, there is no available information in literature regarding deposition of bioactive glass onto such substrate as ultrafine-grained cpTi. In spite of bioactive glasses are characterised by higher bioactivity index than that of HA and their reactivity with existing bone tissue is superior [30].

There are several methods that can be employed to obtain bioactive glass (and/or glass-ceramic) coatings on bioinert metallic substrates. The most popular are enamelling, plasma spraying, electrophoretic deposition and thin film techniques. Enamelling is an easy and inexpensive procedure although it has two significant disadvantages. First, the entire volume of a substrate is maintained at relatively high temperatures. When bioactive glass is coated on titanium or titanium alloy substrates, which are metallic materials most commonly used in the biomedical field, the excessive temperatures may cause degradation of the mechanical properties of the implant due to $\alpha \rightarrow \beta$ transformation of cpTi occurring at the temperature above 885 °C, or above 955 °C in the case of Ti6Al4V alloy [31]. Second, significant residual stresses may arise during the cooling stage of the enamelling process due to mismatch in the coefficients of thermal expansion of glass and metal [32].

In plasma spraying, the bioactive glass powders are injected into the plasma flux, which can reach a temperature higher than 15000 °C at the nozzle exit. The powder particles, being partially or fully melted, impacts onto metallic substrate at a high velocity. The main advantage of the plasma spraying process in comparison with enamelling is that the substrate temperature remains low, which prevents its degradation. Unfortunately, the disadvantage of using a plasma spraying of bioactive powders onto metallic substrates is that the glass coatings have poor adhesion to metal. Additionally, the coatings are often very defective [32].

Electrophoretic deposition is an electrochemical technique, in which electric field is created between two electrodes, one of which is a metallic substrate immersed in a liquid medium. The charged particles are deposited onto this substrate. Progressive accumulation of the particles leads to formation of a relatively homogeneous and compact film [33]. This method allows for coating parts with a complex shape. The main drawback of electrophoretic deposition is that the substrate must be conductive or a conductive film must be imposed on it.

The thin film techniques have been also used to produce bioactive coatings since the early 1990s [34]. The most popular method is pulse laser deposition (PLD) where the high-power pulsed laser beam is focused on a material, which is to be deposited in a vacuum chamber. The material is vaporised, the plasma plume is created and imposed on a substrate as a thin coating, typically between tens of nanometres and several micrometres thick [35]. It has been shown, that after application of the PLD process, the coating composition is very similar to that of the original glass [36]. The main disadvantage of a PLD technique is that it requires vacuum chamber and the deposition rate is relatively low.

One of the most promising methods employed for obtaining bioactive glass coatings on the metal surface is laser cladding [37], in which a laser beam is focused onto the metallic substrate in order to form a melt pool, while bioactive glass in powdered form is delivered onto it by an inert gas. The powder melts and rapid quenching of the molten pool takes place as the laser beam moves further. As a result, a bioactive glass coating is formed on the metallic

substrate. The technique has many advantages due to good deposition rate and due to the fact that the entire substrate is not exposed to high temperatures during the processing. Hence, the ultrafine-grained structure of metallic materials obtained through SPD processing can be preserved. Moreover, despite the noticed glass crystallisation, coatings obtained using laser cladding preserve the bioactivity of the original glass [38]. Laser coating of 45S5 Bioglass® on titanium substrates has been investigated for biomedical implants [39]. Bioactive glass compositions alternative to 45S5 Bioglass® have been used in laser cladding to apply a bioactive glass layer onto the surface of a titanium alloy without the necessity of any previous treatment of the surface [38]. Calcium phosphate (CaP) coatings were also cladded onto pure Ti and Ti alloys. For example, tricalcium phosphate powders $Ca_3(PO_4)_2$ were used to obtain biocompatible coatings on pure titanium [40]. Such composite showed an increase of osteoblastic cell proliferation in comparison with the cpTi substrate alone. CaP was cladded also onto a Ti6Al4V plate and good bonding to substrate as well as positive *in vitro* performance were reported [41]. The main drawback of using the laser cladding method is that the coefficient of thermal expansion (CTE) of the substrate and coating has to be similar to avoid micro-cracks. The processing parameters need to be properly adjusted since even small modifications of the bioactive glass chemical composition can change the CTE [42].

In this study, we discuss application of laser cladding, which was used for the first time to obtain bioactive glass coating on an ultrafine-grained cpTi and report on the selection of the appropriate processing parameters using numerical analysis and also the performance of the coated material in vitro coupled with microscopic investigations. The study's findings demonstrated that obtaining important combination of various layers across the material cross section characterised by different microstructure and properties can have synergistic effect allowing for obtaining remarkable mechanical properties and high bioactivity eventually leading to obtaining biomaterial free from toxic elements that potentially can be used for load bearing medical implants.

2. Numerical Modelling

The computer simulation of laser cladding was carried out for the purpose of selecting appropriate processing parameters. The numerical analysis was intended to help in the determination of such parameters as laser power and scanning speed. Their impact on temperature, crystallinity and porosity was studied. We assumed that the temperature in the whole volume of bioactive glass is to be higher than its melting point just as it takes place in a selective laser melting (SLM) process. The reason for this is that doing so allows for a better bond between the glass and the substrate. This is due to the fact that a relatively large melting zone in the substrate is obtained in which the mixing of the metal with the glass takes place. Moreover, the complete melting of the glass results in obtaining a high relative density in its volume, which is beneficial in terms of cladded track strength [43]. Furthermore, the complete melting, compared to the partial melting of glass, results in its lower tendency to crystallization [44,45].

The analysis of the influence of scanning speed on crystallinity and porosity was also performed. Crystallinity is one of the factors, which affects the bioactivity of such bioactive materials. The high degree of crystallinity increases the onset time of generating the HA surface layer, which is responsible for establishing a biological bond with host tissues [46]. Porosity also affects the bioactivity of medical implants as it improves their ability to bond with host tissues [47].

Summarising the above discussion, the laser power was selected based on the temperature distribution in the glass, so that the temperature of the entire volume exceeds the

melting point. Then, the influence of different laser speeds on the crystallinity and porosity degree was analysed using this laser power. The aim was to select the speeds that would result in a relatively low level of crystallinity and a relatively high level of porosity.

It was planned to clad a single bioactive glass track onto the ultrafine-grained cpTi substrate. For that reason, the finite element (FE) model representing the corresponding set-up was developed and applied for the analysis using Abaqus/Standard software (Fig. 1).

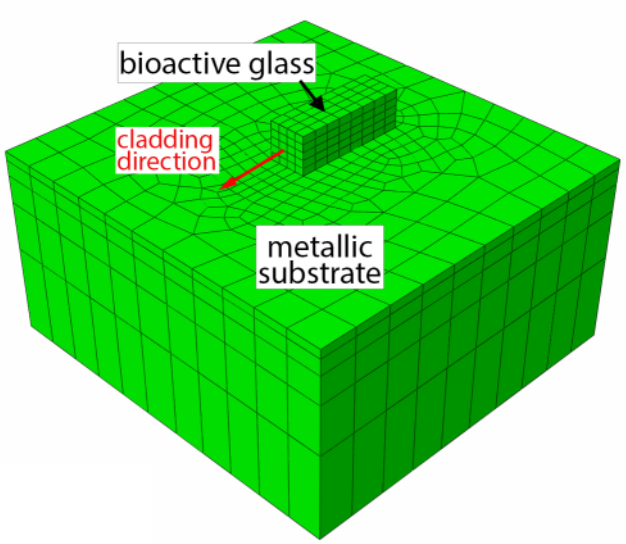

Fig. 1 FE model set-up showing a single bioactive glass track cladded onto metallic substrate.

The model consists of two sets of 3D elements. The first set represents an ultrafine-grained cpTi Grade 4 substrate and the second one represents a S520 bioactive glass material accumulated on the surface of the metallic substrate. In the experimental laser cladding process, the bioactive material is gradually cladded along with the laser beam movement, as is shown in Fig. 7. The numerical analysis takes into account the increase in the amount of bioactive cladding material, using time-dependent activation of the finite elements (also known as birth and death technique) [48]. The cladded layers were represented by finite elements at the stage of model configuration. The corresponding finite elements representing the cladded material were deactivated at the beginning of the numerical analysis. Then, those elements were selectively activated depending on the cladding speed.

The metallic substrate was assumed 10 mm long, 10 mm wide and 5 mm thick. The width and thickness were consistent according to the planned experiment. The assumed length was lower than the corresponding length of the experimental samples. However, it was sufficient for obtaining the reliable numerical results while allowing for lowering CPU time required for the simulation at the same time. A single, 1 mm thick and 1 mm wide, track of S520 bioactive glass was considered in the numerical simulation to match the experimental results. The thermophysical properties of materials used in the modelling are presented in table 2. In case of lack of some material information, data for similar materials, mostly for conventional cpTi Grade 4 and 45S5 bioactive glass, were used. In such cases, or if the corresponding values were estimated, indications “after” were used in table 2.

Table 2 Thermophysical properties of metallic substrate and bioactive glass used in the numerical analysis.

	ultrafine-grained cpTi, t(°C)	**S520 bioactive glass**
Density, kg/m^3	4534 [49]	2700 after [50]
Heat capacity, J/kg °C	for: $25°C \leq t \leq 950°C$: $c = -0{,}0001t^2 + 0{,}2997t + 532{,}1$ for: $950°C < t \leq 1650°C$: $c = 0{,}0002t^2 - 0{,}3444t + 822{,}39$ after [51]	500 after [52]
Latent heat, J/g	360 [53]	-
Melting temperature, °C	1668 [54]	1063 (Fig. 6b)
Effective thermal conductivity, W/m °C	$k = 6 \cdot 10^{-6}t^2 - 0{,}0054t + 21.173$ after [55]	50-90 after [56]
Convection coefficient, W/m^2 °C	50 [51]	50 [51]
Stefan-Boltzmann constant, W/m^2 K^4	$5{,}67 \cdot 10^{-8}$	$5{,}67 \cdot 10^{-8}$
Emissivity coefficient	0,708 [57]	0,92 after [55]

2.1 Laser beam

The laser radiation was defined as a volumetric heat source to be absorbed in a volume of a green body as described by Kongsuwan et al. [39]. Laser energy was described by a Gaussian distribution in the radial direction and exponential decay in the depth direction according the following equation:

$$Q(r,z) = Q_0 exp\left(\frac{-2r^2}{R_0^2}\right)\exp(-\alpha z) \quad (1)$$

where $Q(r,z)$ is the heat flux at point (r,z), Q_0 is the peak flux, R_0 is $1/e^2$ radius of the laser beam on the top surface, and α is the absorption coefficient of the green body. The peak flux Q_0 is defined as follows:

$$Q_0 = \frac{Q_L}{\pi \cdot R_0^2 \cdot d} \quad (2)$$

where Q_L is the laser power and d is the heat penetration depth.

The heat source defined by equation 1 was implemented into the model using DFLUX subroutine. The laser power, the radius of the laser spot and the scanning speed were assumed to be 50 W, 0.5 mm and 1 – 2 mm/s, respectively. The initial temperature of the metallic substrate and cladded material was assumed to be 25°C.

2.2 Crystallization

The phenomenon of crystallization results from nucleation and crystal growth, and it can be mathematically described by using the Johnson–Mehl–Avrami–Kolmogorov (JMAK) equation [58–60]. In laser cladding, nucleation and crystal growth in cladded bioactive material

occur simultaneously and the crystallized volume fraction for nonisothermal condition can be calculated using the following expression [39,61]:

$$X\big(T(t)\big) = 1 - exp\left\{-\left(\int_{t_0}^{t} K\big(T(t')\big)dt'\right)^{d}\right\} \tag{3}$$

where X is the crystallized volume fraction, T is the temperature, t is the time during which the bioactive material experienced laser sintering, K is the temperature dependent crystallization rate, which includes nucleation and crystal growth, and d is the dimensionality of growth. The function of K can be expressed by the Arrhenius equation:

$$K(T) = K_0 \exp\left(-\frac{E_c}{RT}\right) \tag{4}$$

where K_0 is the pre-exponentials of crystallization rate, E_c is the activation energy for crystallization, R is the gas constant and T is the absolute temperature. It has been assumed in the modelling that $E_c = 280$ kJ/mol [62] and R = 8,314 J/mol*K.

2.3 Porosity

The overall porosity P is calculated using the following equation [39]:

$$\mathrm{P} = 1 - \left\{\rho_i + (1-\rho_i)\Psi - F_{pore}[1-\rho_i-(1-\rho_i)\Psi]\right\} \tag{5}$$

where ρ_i is the initial density of the powder, Ψ is the sintering potential and F_{pore} is the pore growth factor. The ρ_i has been assumed to be 57,5% [63].

The sintering potential Ψ provides information about the sintering state of the material and is in the range of [0;1). The value $\Psi = 0$ corresponds to loose powder, while Ψ tends to be 1 in fully sintered material (with relative density equal to 1). The sintering potential Ψ can be calculated by the expression given in [64]:

$$\Psi\big(T(t)\big) = 1 - exp\left\{-\int_{t_0}^{t} \zeta\big(T(\tau)\big)d\tau\right\} \tag{6}$$

where ζ is the sintering rate. A model developed elsewhere [65] expresses the sintering rate:

$$\zeta(T) = \frac{\gamma(T)}{\eta(T)d_0} \tag{7}$$

where γ is the surface tension or surface energy, η is the viscosity of the heat-treated material and d_0 is the characteristic length scale of the initial material. The γ was assumed to be 54,7 mN/m [66]. In the case when glass is partially crystallized, the viscosity changes depending on degree of crystallization and viscosity of the amorphous glass. The effective viscosity can be obtained using Einstein-Roscoe expression [39]:

$$\eta_{ef}\left(X\big(T(t)\big)\right) = \eta(T)\left(1 - \frac{X\big(T(t)\big)}{X_{max}}\right)^{-n} \tag{8}$$

where X_{max} and n are adjustable parameters and the standard values $n = 2{,}5$, $X_{max} = 0{,}75$ were assumed for the modelling [67]. Accordingly, the sintering rate ζ has to be modified to take into account the phenomenon of crystallization [68]:

$$\zeta(T) = \frac{\gamma(T)}{\eta_{ef}\left(X\left(T(t)\right)\right) d_0}\left(1 - X\left(T(t)\right)\right) \tag{9}$$

During the sintering, there is a possibility that an isolated pore will diffuse and coalesce with the neighbouring pore. The rate of pore growth related to diffusion and coalescence is given by [68,69]:

$$\frac{dr_p}{dt} = \frac{mD_p\gamma(T)v_p}{r_p^2 k_b T} \tag{10}$$

where r_p is the pore radius, m is the constant, D_p is the pore diffusion coefficient, γ is the surface energy, v_p is the pore molar volume, k_b is the Boltzmann constant and T is the absolute temperature. The pore growth factor F_{pore} may be expressed as a function of final pore radius r_f and initial pore radius r_i [39]:

$$F_{pore} = \frac{r_f^3 - r_i^3}{r_i^3} \tag{11}$$

2.4 Selection of experimental parameters using numerical analysis

Taking into consideration the obtained simulation results, the laser power was determined to be 50 W, as this value allowed to reach temperatures higher than the melting point of glass in the whole volume of the cladded track for the entire speed range.

The crystallinity distribution in bioactive material obtained after the laser cladding for different scanning speeds was presented in Fig. 2. The volume fraction of crystallized phase after the processing equals 23.1% for 1 mm/s laser speed (Fig. 2a). The increase of laser velocity by 33%, up to 1.5 mm/s, caused reduction in crystallized fraction, decreasing it to 8% (Fig. 2b). Further increase of the scanning speed up to 2 mm/s resulted in even lower crystallinity level of 4.8% (Fig. 2c). It favoured the conclusion that the increased laser speed allows for significant reduction of crystallinity, which can be considered as beneficial, because it decreases the onset time of generating the HA surface layer.

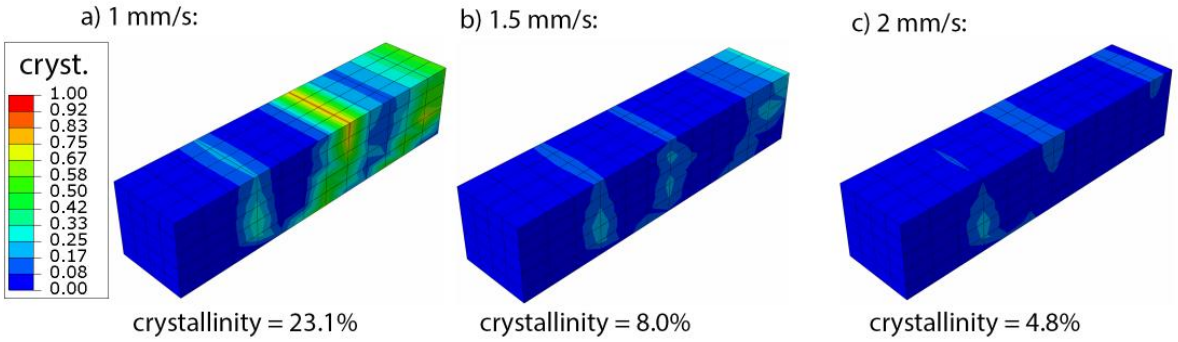

Fig. 2 Crystallinity distribution in bioactive glass after the laser cladding process with laser power of 50 W and various scanning speed: a) 1 mm/s, b) 1.5 mm/s, c) 2 mm/s.

Fig. 3 shows the porosity distribution in bioactive glass predicted after the laser cladding assuming various laser beam velocities. The highest level of porosity (18.2%) was achieved for the greatest laser speed (Fig. 3c). The lowest pore volume fraction (9.4%) was obtained in the case of the lowest velocity of the laser beam (Fig. 3a). It can be seen in Fig. 3b, that when the scanning speed was equal to 1.5 mm/s, the porosity level was 16.2%. It can be noticed, that the most favourable for obtaining high level of porosity is using higher laser speeds.

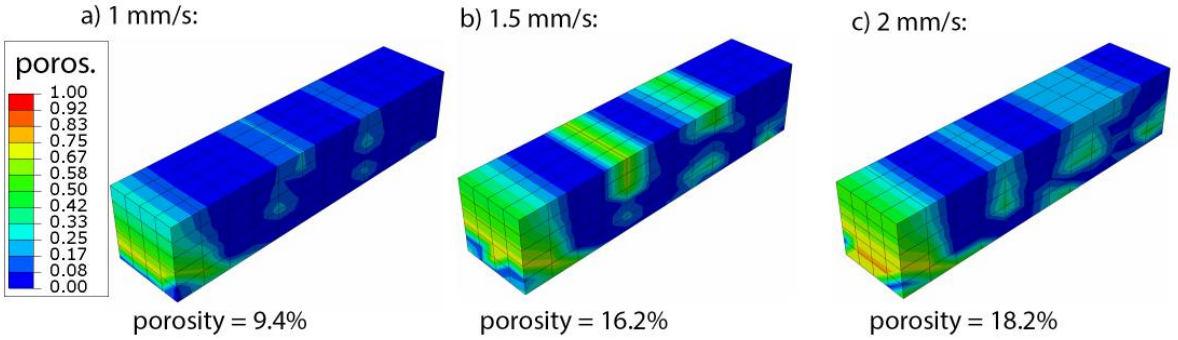

Fig. 3 Porosity distribution in bioactive glass after the laser cladding process with laser power of 50 W and different scanning speed: a) 1 mm/s, b) 1.5 mm/s, c) 2 mm/s.

There is significant difference in crystallinity degree between 1 mm/s and higher values of scanning speed. However, the crystallinity level is rather low for both 1.5 and 2 mm/s speeds. At the same time, the achieved levels of porosity are comparable at the higher speeds. Therefore, taking into account the stability of the process, we decided to use a speed of 1.5 mm/s in the following experiments.

3. Materials and methods

3.1 Bioinert substrate

The commercially pure titanium (cpTi) Grade 4 was used to produce the ultrafine-grained substrate. The chemical composition of the material, in wt.%, is 0.05C, 0.15Fe, 0.05N, 0.007H, 0.36O, residuals<0.3, and Ti as the balance. In the initial state (upon receipt), the material had an average grain size of 25 μm. Before deformation, annealing at the temperature

of 680°C for one hour was carried out as heat treatment. Then, the workpiece was subjected to equal-channel angular pressing combined with the Conform process (ECAP-C) [70,71]. The material was deformed on 6 ECAP-C passes through the Bc route whereby the bar was rotated 90° clockwise after each subsequent pass. Before each pass of the ECAP-C, the workpiece was heated in a furnace at a temperature of 200°C for 15 minutes. Then, it was immediately placed in the tooling of the deformation unit, which had also been heated up to the temperature of 200°C. Finally, the bar acquired 11 mm × 11 mm square cross section. Additional heat treatment after deformation was not applied.

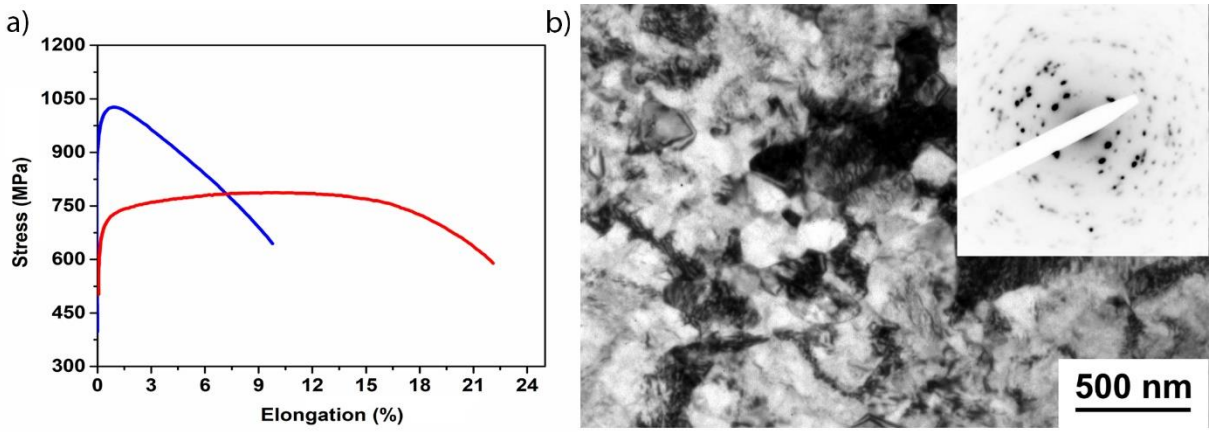

Fig. 4 Tensile stress-strain curves of cpTi Grade 4 after ECAP-C (blue line) in comparison to its coarse-grained counterpart (red line) (a) and TEM micrograph illustrating cpTi Grade 4 microstructure after ECAP-C (b).

There has been a significant relative increase in the strength of cpTi Grade 4 samples after ECAP-C in comparison to their coarse-grained counterparts. The ultimate tensile strength reached the values of the well-known titanium alloy Ti-6Al-4V ELI, exceeding 1000 MPa (Fig. 4a). This is accompanied by a decrease in ductility, which is typical for deformed metals. The reported increase of the titanium strength is strongly associated with reduced size of structural elements such as grains and sub-grains. The microstructure of the obtained material after ECAP-C is characterised by the relatively large grains, not exceeding 5 μm, and fine grains/sub-grains with sizes of about 300 nm (Fig. 4b). The shape of the observed structural elements is elongated in one direction that is a distinctive microstructural feature of metals subjected to ECAP with a relatively low degree of deformation at low temperatures. The small equiaxed grains were observed in various areas along with the elongated grains.

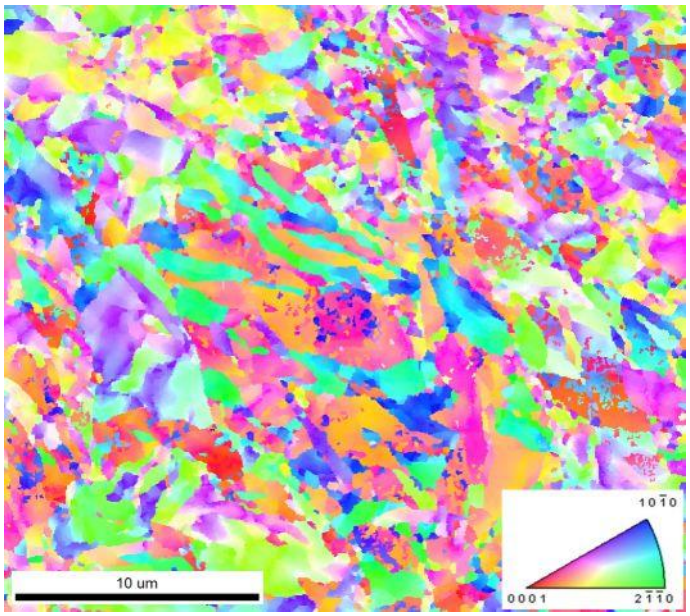

Fig. 5 EBSD inverse pole figure map showing the microstructure in transverse cross-section of the severely-deformed bar.

Fig. 5 illustrates EBSD inverse pole figure map showing highly refined microstructure of the cpTi Grade 4 after ECAP-C. It can be seen, that small grains of irregular and elongated shape predominate. Since the obtained material is going to be used potentially for load bearing medical devices (implants), its most important properties are those related to the mechanical performance, and the mechanical properties are largely related to the anisotropy in microstructure [72,73]. This may be advantageous in some cases, e.g. when the implant is subjected to much higher loads in a given direction. However, when dealing with other cases, such material with an anisotropic microstructure may be heat treated to randomize the crystallographic texture and reduce anisotropy in mechanical properties. In this work, however, we wanted to investigate what effect the laser beam would have on the irregular microstructure, so the material after such severe plastic deformation (SPD) treatment was directly subjected to laser cladding without applying heat treatment.

3.2 Bioactive glass powder

S520 bioactive glass powder with composition presented in table 1 was synthesized by melt – quenching method. The glass batch was prepared by mixing appropriate amounts of silicon dioxide (SiO2, AR, POCh, Poland), phosphorus pentoxide (P2O5, AR, Sigma-Aldrich), calcium carbonate (CaCO3, AR, POCh, Poland), sodium carbonate (Na2CO3, AR; POCh, Poland), sodium carbonate (K2CO3, AR; POCh, Poland) using a SpeedMixer (FlackTekInc, USA). The homogenized powder was melted in the electric furnace at 1450°C for 2 h in a platinum crucible. The molten glass was poured into cold water to obtain glass frit and subsequently dried to a constant weight. The glass frit was milled in the planetary mill (Pulverisette 6, Fritsch) using zirconia grinding bowl and ball and sieved to obtain the bioglass powder with particle size in the range of 100-200 μm.

The S520 powder was chosen, as it shows smoother wetting angle-temperature behaviour than 45S5 and was successfully used in laser cladding processes to produce bioactive glass coatings in the past [38].

Table 1 Composition of the S520 bioactive glass powder.

	SiO_2	Na_2O	CaO	K_2O	P_2O_5
nominal mol, %	52	20.9	18	7.1	2
mol, %	51.8	19.4	19.3	7.4	2.1
wt.%	48.7	18.7	17	10.9	4.7

X-ray diffractometry (XRD) analysis was performed using PANalytical X-ray Diffractometer X'Pert Pro in the 2θ range of 10–90° with CuKα radiation source and 0.008° step size. Results presented in Fig. 6 indicate the pattern shape typical for the amorphous phase (broad humps at 2θ: around 25–35°, at around 50-60°) and no crystalline peaks occur. The differential scanning calorimetry (DSC) analysis indicates that the transformation temperature T_g is 483°C (Fig. 6b). The double exothermic effect from crystallization (T_{c1} - 622°C and T_{c2} - 702°C) may be associated with the presence of two amorphous phases with a different tendency to crystallization, or with the further crystallization or crystallographic modification of the lower temperature (T_{c1}) crystal phase. The melting temperature (T_m) of the glass is 1063°C.

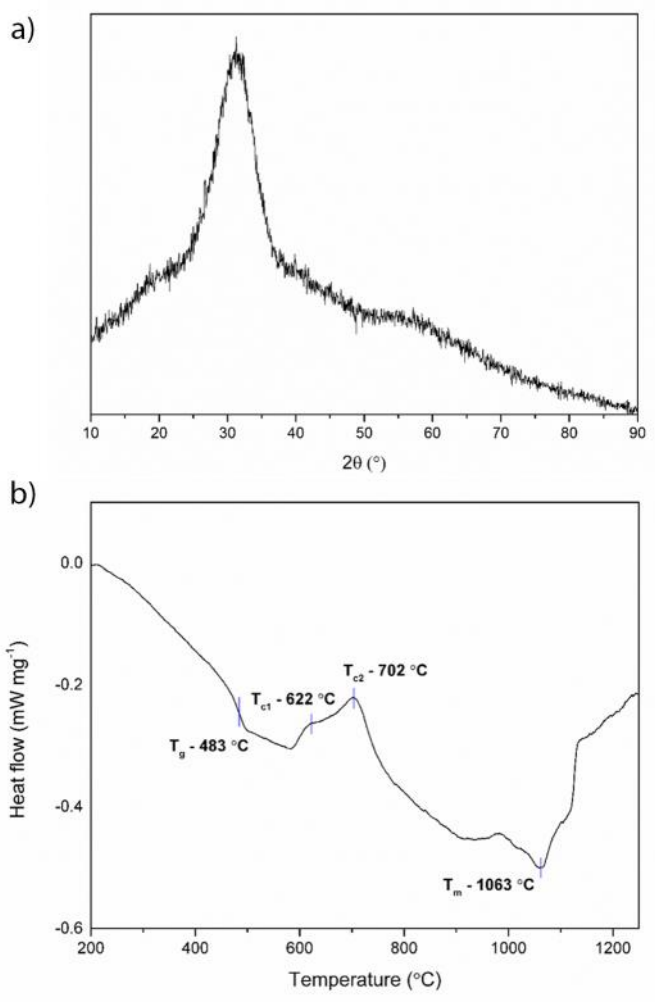

Fig. 6 XRD diagram (a) and DSC plot (b) of the obtained S520 bioactive glass powder.

3.3 Laser cladding of glass powder onto bioinert substrate

Ultrafine-grained cpTi bars were cut in half along the cross-section using a slow speed diamond saw. The titanium sample surface was cleaned with acetone before laser cladding. A

hybrid laser direct energy deposition (DED) system was used for laser cladding of the synthesized S520 bioactive glass onto ultrafine-grained cpTi substrate. Although, the system allowed for application of multiple tracks on the surface of the metallic basement, as shown in Fig. 7b–c, the consideration is limited to a single track in this study. The aim of this approach is to gain a detailed understanding of the interrelated phenomena occurring during the application of a single track. It will clear the way and facilitate further studies to understand and optimise the microstructure evolution in both the substrate and glass during cladding of multiple tracks. The hybrid laser DED system consists of a 5-axis Mikron 450u, which is integrated with a retrofitted laser deposition system and a multi-materials powder delivery system. The laser source has a fundamental wave length of 1064 nm and maximum output power of 1200 W. High purity argon gas was used as the powder delivery and the side shielding gas. The volumetric flow of the powder carrying gas and the shielding gas was set to around 2-5 l/min, and 5-10 l/min, respectively, in order to provide a continuous powder flow and maximum protection of the titanium substrate from oxidation. The laser beam was focused on the substrate surface at 5 mm focus length. The laser spot size was 1 mm in diameter. The working head consisting of laser optics and a powder injection system was docked together and it was fixed at a position with the substrate moving at a scanning speed of 1.5 mm/s under a laser power of 50 W. The bioactive glass powder particle sizes of 100 - 200 µm were chosen to ensure a good flowability during the whole process. A schematic diagram of the laser cladding process is shown in Fig. 7a.

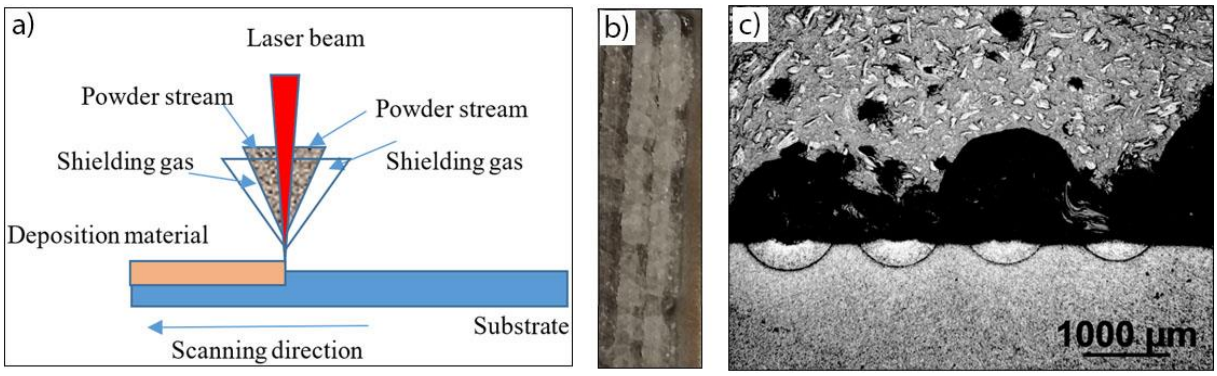

Fig. 7 Schematic representation of the laser cladding process (a), coating consisted of many tracks cladded onto ultrafine-grained cpTi substrate (b) and optical micrograph showing cross-section of the bioactive glass tracks coated onto ultrafine-grained cpTi (c).

3.4 Microstructure characterization

The bioactive glass-coated ultrafine-grained cpTi samples were cut along the cross-section using low speed diamond saw in order to avoid stress induced cracking. Next, the samples were prepared for microstructure characterization by initial grinding on abrasive papers (SiC) and mechanical polishing on cloths. The specimens were examined by light microscopy as well as by scanning electron microscopy (SEM) with back scattered electrons (imaging and diffraction – EBSD). In addition, chemical analysis by energy dispersive X-ray spectroscopy (EDS mapping) was performed in the SEM. All microstructural examinations were carried out on a Zeiss Axio Imager M1m light microscope and on a high resolution FEI Nova NanoSEM scanning electron microscope equipped with a field emission gun and an EDAX system for chemical analysis.

Hardness measurements were conducted on the sample cross-sections using a Vickers microhardness tester with 25 g indentation load and 10 s dwell time. A distance between two

neighbouring indentations was established to at least 25 μm in order to prevent inaccurate measurements resulted from the affected plastic zone in the vicinity of an indent.

3.5 In vitro bioactivity test

In vitro bioactivity of glass coatings was investigated by samples incubation in SBF as described by Kokubo & Takadama [74]. The length of the specimens after the laser cladding process was above 100 mm. The specimens needed to be cut into smaller parts before immersion in SBF and further studies. In order to carry out the cutting, the bioactive glass layer would need to be coated with resin to protect the layer from falling off during the cutting process. Subsequent removal of the resin for testing would be quite cumbersome and could affect the texture/structure of the bioactive glass, or even damage the coatings, and therefore could affect the test results. Since the experiments were aimed to assess the bioactivity of the coating after the laser cladding, we decided to separate the cladded layer to avoid an effect of Ti basement on the results of testing in SBF. Hence, the chunks of bioactive glass were pulled off from the ultrafine-grained cpTi substrate, immersed in SBF and incubated at 37°C for 3, 7 (data not shown) and 14 days. The ratio of the glass sample weight (g) and solution's volume (ml) was 1/100. Afterwards the samples were taken out of SBF, washed in pure ethanol and air dried at 25°C.

Before and after bioactivity test the samples structure was examined using FTIR and Raman spectroscopy. FTIR spectra were recorded with the Bruker Vertex 70v spectrometer. Samples (glass powder and coating) were prepared by the standard KBr pellet method. Spectra were collected in the middle infrared 4000–400 cm-1 range (MIR), and 128 scans were accumulated at 4 cm-1 resolution. Raman studies were conducted using HoribaLabRAM HR micro Raman spectrometer. The exciting 532 nm laser power was set to 15 mW. The 1800 gr/mm grating with 100x objectives were used and 2 scans of 300 s each were accumulated.

Surface morphology and chemical analysis of samples before and after mineralization in SBF were tested with the use of scanning electron microscopy SEM (Nova NanoSEM 200 FEI Europe Company, accelerating voltage 15 kV) coupled with an energy dispersion X-ray (EDX) analyzer. Based on a semi-quantitative analyses of the EDX spectra collected from at least three different points of each sample the Ca/P molar ratios of the layers formed on glass coatings were calculated. The changes in Ca, P, Si concentration in the SBF during sample immersion were monitored using an ICP-OES technique (Plasm 40, Perkin Elmer, USA).

4. Results and discussion

4.1 Microscopic Examination

A single S520 bioactive glass track was cladded onto ultrafine-grained cpTi substrate and the cross-section of such multi-layered material was shown in Fig. 8. The ImageJ software was used to analyse the obtained microstructures. The mean width of the track is around 1.2 mm, the thickness is around 1 mm and the porosity level is around 15%, which equals relative density of about 85% (Fig. 8a) and is close to the results of numerical analysis (Fig. 3b). Two characteristic areas can be seen in substrate below the cladded track (Fig. 8b). The first one is localized directly under the track and is about 50 μm deep and above 300 μm wide. The second one surrounds it and is about 125 μm deep and about 450 μm wide. The results presented later in this article indicate that these are melted area and part of the heat affected zone (HAZ), respectively. It can be seen, that the microstructure was significantly affected in the melted area and in HAZ, however other techniques, such as SEM, are necessary to precisely identify changes in this region.

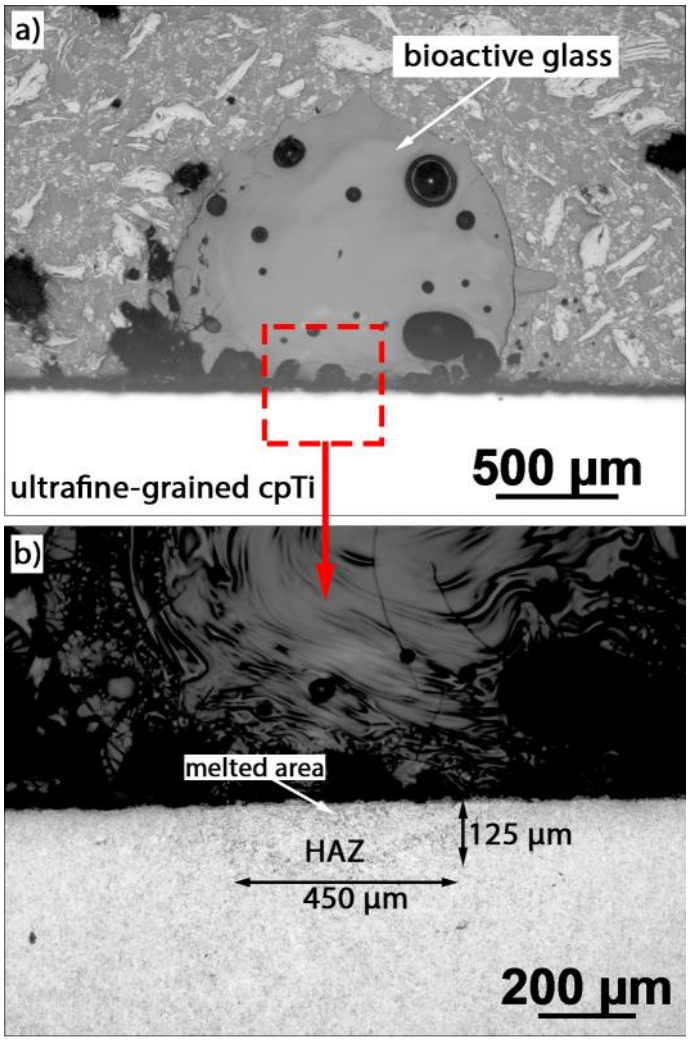

Fig. 8 a) Cross-section of the bioactive glass coating (single track) on ultrafine grained cpTi substrate, b) melted area and part of the heat affected zone (HAZ) under the cladded track.

Low-energy-input laser processes may induce high cooling rates, in the range of 1000-10000 °C s^{-1} [75], hence extensive microstructural changes can be expected in affected areas. SEM was used to analyse various zones of melted and HAZ areas. The images of different regions were put together and presented in Fig. 9.

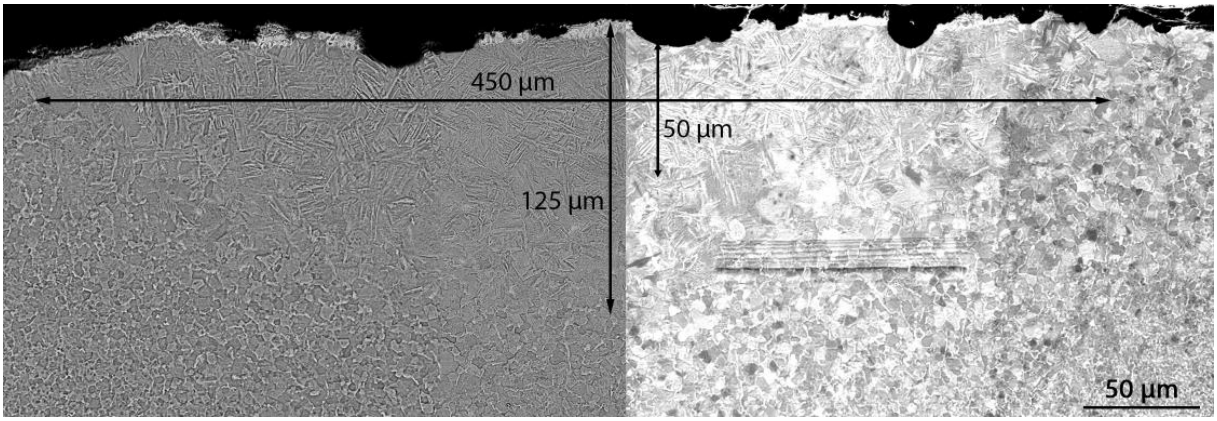

Fig. 9 Combination of three cross-sectional SEM images, showing melted and HAZ areas (HAZ is deeper than 125 µm - it also contains small recrystallised grains at greater depths).

It can be seen, that the heat from laser beam had a significant impact onto the ultrafine-grained cpTi microstructure. The α' acicular martensite was identified in the melted area. At greater depths, in HAZ, it gradually passes into grains of relatively high diameter of approximately 10 µm as is shown in Fig. 10. Then, these grains pass into smaller ones with a regular shape and diameter of about 2 µm. These grains significantly differ in shape from those of the original microstructure presented in Fig. 5, which may indicate, that heat affected them, and hence they arose as a result of recrystallization. Thus, it seems that HAZ reaches deeper than it appears from optical micrograph (Fig. 8b) – even deeper than 200 µm from the surface. As it was mentioned earlier, the substrate after the SPD processing had grains mainly of irregular and elongated shape. The laser beam influenced that microstructure transforming it in melted and HAZ areas, hence, the overall volume of the original irregular microstructure decreased at the expense of acicular martensite formation, which gradually passes with depth into regular highly refined grains. The α' phase formed in a coarse-grained microstructure improves the tensile strength and hardness and decreases plasticity [76]. This is not happening in the case, where the original microstructure was highly refined. The results of hardness measurements, presented further in the article (Fig. 12), showed that the hardness of acicular martensite is lower than hardness of the original microstructure. It indicates that plasticity may be higher in the melted area. Moreover, the highly refined grains in HAZ have hardness comparable to that of the original irregular microstructure. At the same time, the grains are axisymmetric and therefore free from disadvantages associated with anisotropy of properties. Such a combination of various properties may have synergistic effect, which may be beneficial for the biomaterials produced.

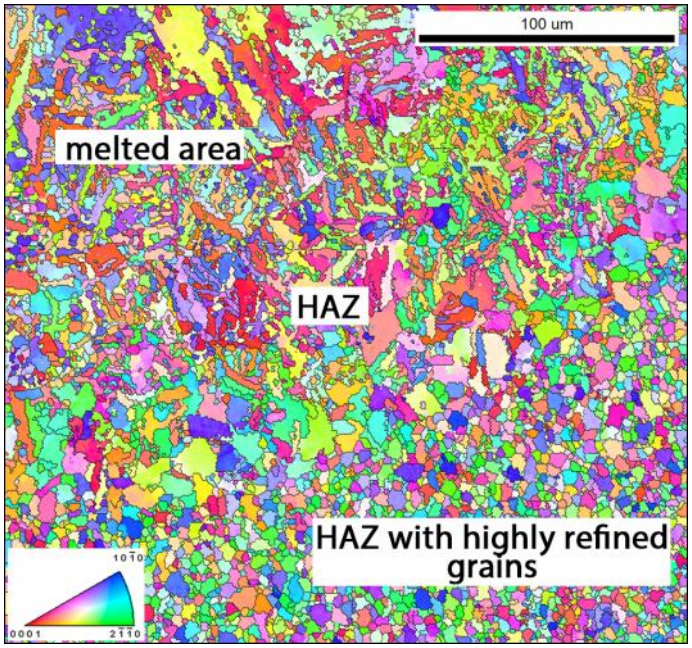

Fig. 10 EBSD inverse-pole-figure map of the cross-section showing melted and HAZ areas resulting from the influence of the laser beam.

SEM image and EDS elemental mapping of the cross-section of the bioactive glass coating onto ultrafine-grained cpTi substrate are presented in Fig. 11. A characteristic region, in the form of a band about 3 μm wide, pointed by the white arrow in Fig. 11a, is formed in the melted zone about 10 μm below the Ti surface. The EDS analysis shows that the Ti content is lower in this zone (Fig. 11b). At the same time, there are certain amounts of Si and Na present in this area (Fig. 11c-d). Titanium Grade 4 does not contain Si or Na, which indicates that these elements were moved from the glass to the substrate. S520 bioactive glass contains 17 wt.% CaO and 4.7 wt.% P_2O_5, however Ca was not found in the considered zone (Fig. 11e), whereas some amounts of P were detected (Fig. 11f). Comesaña et al. [38] used laser cladding to produce S520 bioactive glass coating on Ti6Al4V substrate. They performed EDS microanalysis to obtain composition profiles within the coating cross-section and reported that composition of the bioactive glass coating is not dependent on the depth. Furthermore, they observed a reduced amount of all measured elements at the glass/substrate interface. The more detailed analysis allowed them to measure the content of elements within the substrate surface layer 5 μm below the interface and in the bioactive glass coating, between 2 and 10 μm above the interface. They have not found bioactive glass elements at 5 μm below the substrate surface. Similarly, we have not found them at this depth. However, as can be seen in Fig. 11, there is a band at about 10 μm below the interface that contains some glass elements. The EDS analysis performed by Comesaña et al. did not show any presence of Ti in the glass coatings while more sensitive X-ray fluorescence (XRF) analysis showed small amount of Ti (1.5 wt.% of TiO_2) incorporated from the surface. The results of our EDS analysis have also shown no Ti in the coating (Fig. 11b) favouring the assumption that either Ti is not present in the glass or the EDS spectroscopy is not sensitive enough to detect it. Kuo et al. [77] performed laser cladding of 45S5 bioactive glass onto Ti6Al4V substrate and conducted EDS analysis to obtain elemental distribution in the cross-sectional region of the bioactive glass-coated Ti6Al4V alloy. They found about 7% of Ti and about 30% of Al in the bioactive glass coating at about 20 μm above the interface. It favours the conclusion that small amount of Ti can be transferred into the layer of glass during

laser cladding. In our case, the lower content of Ti registered by the EDS analysis certainly is the result of transition of the glass elements into the substrate, but may also be partly due to transition of small, not detectable by the EDS analysis, amount of titanium into the glass. Kuo et al. showed that Al is excessively transferred into bioactive glass that potentially can be toxic when the glass begins to dissolve in the human body. Moreover, the increasing amount of substrate elements in the coating reduces the average content of Na and P in the bioactive glass, which leads to decreasing the overall bioactivity. It is yet another argument in favour of using pure titanium for load bearing implants. Kuo et al. also noticed that there is a relatively high amount of Si at around 12 μm below the interface. Its amount is higher than in glass at about 20 μm above the interface. This observation is in good agreement with our EDS elemental mapping for Si, where Si can be observed at the same depth from the interface (Fig. 9c). Kuo et al. have also found, that the titanium content at around 12 μm below the substrate surface is reduced by more than 10 percent compared to its content in the core of the substrate. We have also observed reduced amount of Ti at 10-12 μm below the interface (Fig. 11b).

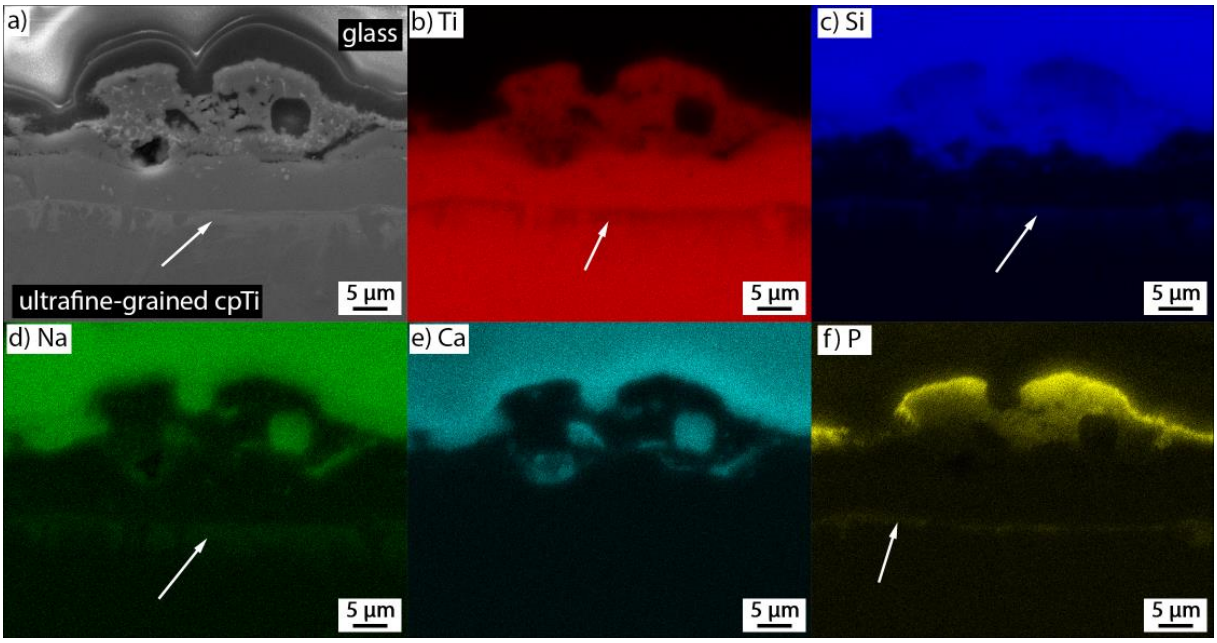

Fig. 11 a) SEM image obtained at the cross section of the S520 bioactive glass cladded onto titanium substrate, b-f) EDS elemental mapping for Ti, Si, Na, Ca and P.

4.2 Hardness measurements

The Vickers micro-hardness tester was used in order to perform hardness measurements on the specimen cross-section. The substrate core hardness was determined to about 315 HV. Fig. 12a presents the optical micrograph, which shows melted and HAZ zone at which three different coloured lines were plotted. Hardness measurements were performed along these lines. The red line indicates the path where the hardness values along the depth were obtained. Three indentations were applied at the same depths from the surface and the obtained values were averaged. It can be seen that just below the surface, at 15 to 50 μm depth, hardness is in the range of 275 – 290 HV, and at a depth of 50 to 125 μm, the hardness falls to around 265 HV (Fig. 12b). The indentations at 15 – 50 μm depth had an irregular shape that can indicate high anisotropy of the structure in that region. Increased hardness may result from a large amount of martensite in this area. After exceeding the distance of 125 μm below the surface,

the hardness begins to increase to the same level as in the substrate core, which is around 315 HV.

Fig. 12c presents microhardness variation along the lines passing through the HAZ. In this case only one indication was applied at each width. It was not possible to perform more tests because they would have had to be performed at different distances from the surface, at which the width and structure of the HAZ is significantly different. The results represented by orange curve were obtained at 75 μm below the surface. It can be seen that width of the zone of reduced hardness is about 450 μm. The hardness values are significantly lower at 150 μm from the left end of the line to 600 μm from it. Similar measurements were performed at the depth of 125 μm below the surface, as pointed by black horizontal line in Fig. 12a. In this case, the width of melted and HAZ is about 250 μm at 250 μm from the left end of the line to 500 μm from it. The bioactive glass track is about 1 mm wide and the zone of reduced hardness observed at 75 μm below the surface is about 450 μm wide. The HAZ and melted zones are probably wider than 500 μm directly below the surface. Hence, it can be seen that over 50% of the glass track is in contact with either HAZ or melted zones. That value may be increased or decreased by modifying the laser processing parameters. The coating adhesion may be increased by reducing the interfacial stresses influenced by CTE mismatch. Verné et al. [78] added 5 wt.% of titanium oxide to bioactive glass powder and produced a titanium-bioactive glass composite on a Ti-6Al-4V substrate. Thanks to this, it was possible to reduce the residual stresses resulted from CTE mismatch. Based on these observations, it can be assumed that the greater contact area between the glass track from one side and the HAZ and melted zones from another one may be beneficial increasing adhesion between the bioactive glass coating and the substrate due to certain amounts of titanium that are transferred from the substrate to the coating reducing the CTE mismatch.

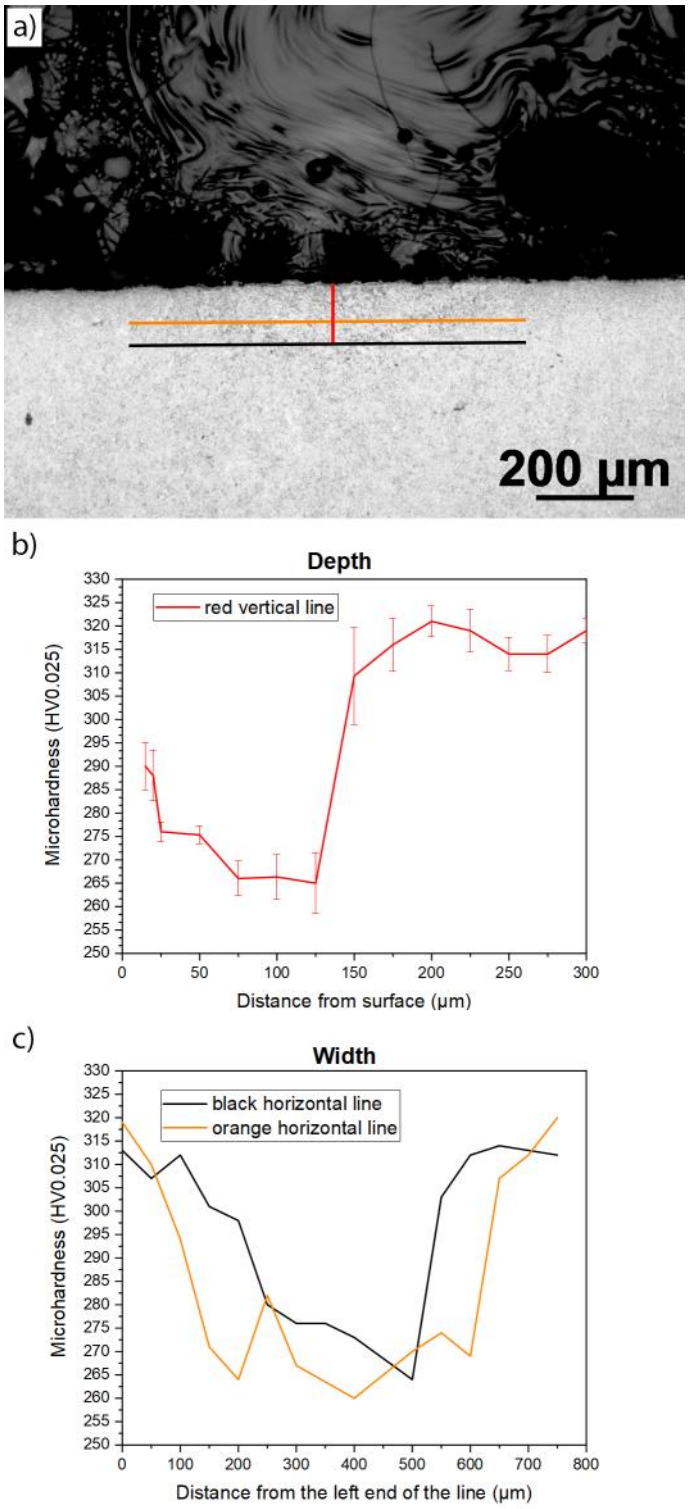

Fig. 12 Variation of the cross-sectional Vickers microhardness in HAZ and melted area beneath the cladded bioactive glass track, a) three plotted onto optical micrograph lines along which hardness measurements were performed (orange line – 75 µm below the surface, black line – 125 µm below the surface), b) microhardness variation along the depth, c) microhardness variation along the width.

4.3 In vitro biomineralization

Raman and Fourier transform infrared (FTIR) spectroscopy were used to analyse the structural changes that occurred in S520 bioactive glass after laser cladding and 14-day immersion in SBF (Fig. 13).

No differences were observed in the Raman spectra recorded for S520 bioactive glass powder and the coating on ultrafine-grained cpTi substrate before the immersion (Fig. 13a). Two broad bands related to Si-O-Si were observed at 610 (rocking) and 1080 cm^{-1} (stretching). Another two bands can be seen at 870 (of relatively low intensity) and 945 cm^{-1}. They are related to non-bridging oxygen (NBO) presence in Si-O(2NBO) and Si-O(NBO), respectively. Del Val et al. [79] have also carried out a laser cladding of S520 bioactive glass to produce three-dimensional multi-layered glass implants. They used different laser parameters, namely the wavelength was $\lambda = 1.6$ μm and the laser power was 18 W. Despite this, they have observed very similar results.

FTIR spectra of bioactive glass powder and bioactive glass coating are displayed in Fig. 13b. Two bands related to stretching vibration modes of Si-O and Si-O(2NBO) are visible at 1050 and 920 cm^{-1}. Comparable bands were identified by Comesaña et al. [80] who used laser cladding to produce three-dimensional S520 and 45S5 multi-layered glass implants. In other studies Comesaña et al. [38] used laser cladding technique to obtain S520 coating on titanium alloy Ti6Al4V substrates. In this case, the broad band at 1050 cm^{-1} was decomposed into two peaks which is due to crystallization. We did not observe such band decomposition, which may suggest that the crystallization has occurred to a lesser extent. However, for S520 bioactive glass powder a single broad band representing Si-O-Si (bend) at 500 cm-1 was observed and after the laser cladding this band split into two bands at 445 and 523 cm-1. It may be attributed to the development of a crystal phase [81].

HA-specific Raman spectra were detected after material incubation in SBF for 14 days (Fig. 13c). No spectral bands characteristic for glass were observed on these spectra, which means that the HA layer covered the analysed materials tightly. The presence of HA layer was indicated by the new bands appeared in the Raman spectra, mainly by strong band at 960 cm^{-1} derived from symmetric stretching vibration of P-O bond in the $[PO_4]$ groups in crystalline HA. Apart from the main peak at 960 cm^{-1}, the P–O asymmetric stretching is also present in the band 1073 cm^{-1} and the shoulder at 1050 cm^{-1}. The band 1073 cm^{-1} can be also attributted to the symmetric stretching mode in the $[CO_3]$ group which suggest the carbonate substitiution in the anionic sub-structure of the crystallized HA. Additionally, the bands at the ranges 430-450 cm^{-1} and 565-610 cm^{-1} corresponding to bending mode of the P-O and O-P-O bonds in the $[PO_4]$ groups, respectively, indicate the crystallization of HA [82].

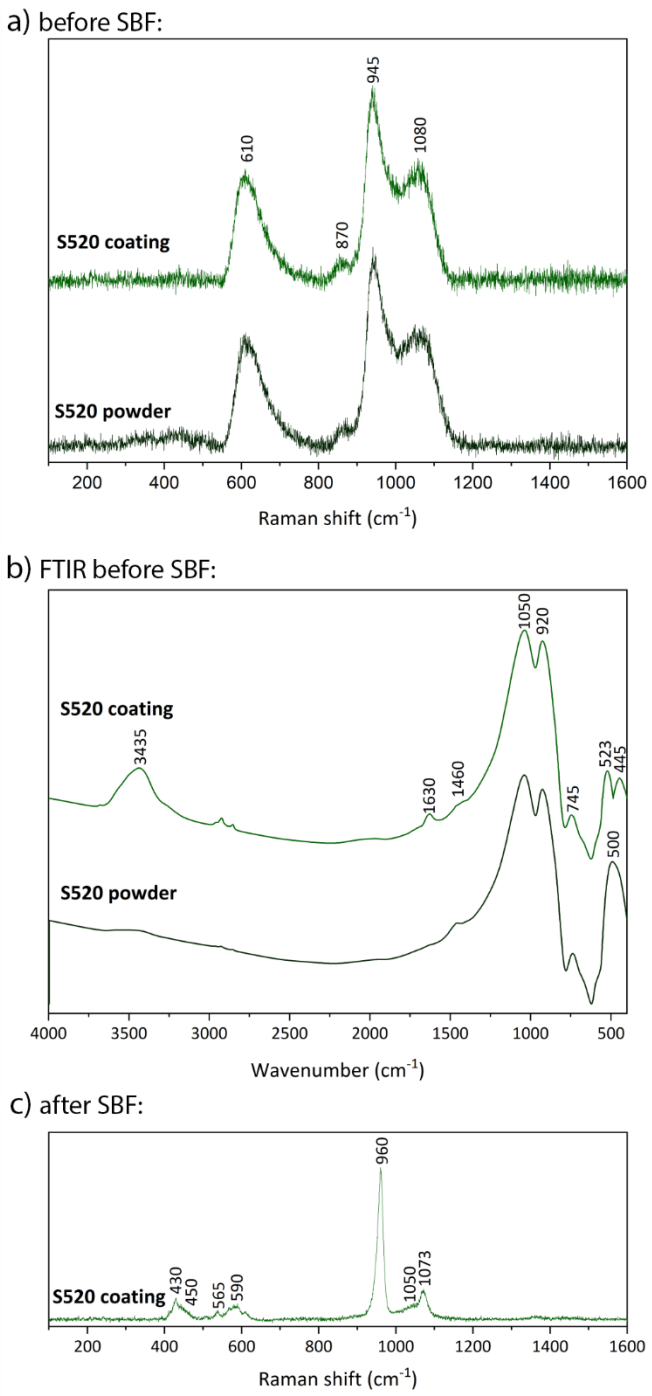

Fig. 13 Raman spectra of the bioactive glass powder and bioactive glass coated onto the ultrafine-grained cpTi substrate before (a) and after 14-day immersion in SBF (c), b) FTIR spectra before the immersion in SBF.

Inductively coupled plasma - optical emission spectrometry (ICP-OES) analysis of the incubation fluid was performed and the results were presented in Fig. 14. Changes in P concentration in SBF during a 14 – day incubation of materials indicate the formation of a HA layer on their surface - a decrease in P content in solution results from its inclusion in the HA layer (Fig. 14a). An almost complete decrease in P concentration after 14 days indicates high bioactivity of materials. Such ion release profile for S520 bioactive glass is in agreements with

study reported in [79]. A significant increase in Ca levels was observed, which indicates rapid dissolution of glass (Fig. 14b). Slowing down the process of Ca release into solution after 3 days indicates the formation of HA layer (inhibition of glass dissolution, inclusion of Ca into the layer). The slowing down of the release of Si to incubation fluid also confirms the formation of the HA layer (inhibiting further glass dissolution). Differences in kinetics of changes of Ca, P and Si concentration in SBF between S520 glass powder and coating were observed, which results from the form of samples (powder/bulk) and thus surface development.

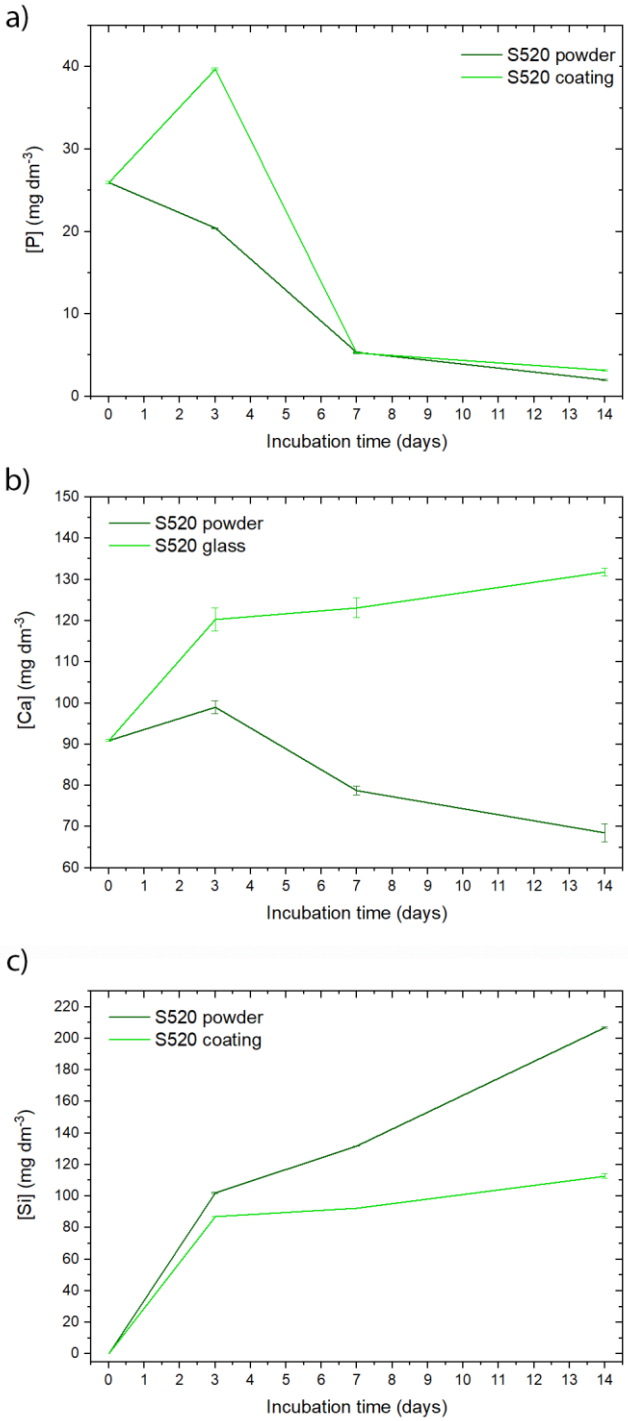

Fig. 14 Variation of P (a), Ca (b) and Si (c) concentration with incubation time in SBF for bioactive glass powder and bioactive glass coated onto the ultrafine-grained cpTi substrate.

The SEM and EDS analysis were performed in order to evaluate the behaviour of bioactive glass coated onto ultrafine-grained cpTi substrate after immersion in SBF (Fig. 15). The SEM analysis showed that after only 3 days of incubation of bioactive glass coating, a calcium phosphate (CaP) layer is formed (Fig. 15b, e). A change in the morphology of the forming CaP layer during incubation is visible. After 14 days, cauliflower-like forms characteristic for HCA can be observed. The elemental composition of the surface also changes - there is an increase in Ca and P content and a decrease in Si. This indicates the increasing thickness of the HA layer being formed, covering the entire surface of the bioactive glass coating. A small content of Na, Mg and Cl is detected in the apatite layer. Comesaña et al. [38] reported similar results for S520 bioactive glass coating deposited onto Ti6Al4V substrate. Peddi et al. [83] developed bioactive borate glass coatings for Ti6Al4V alloy using enamelling technique. They reported that a calcium phosphate rich layer was formed on the glass coating surface. EDS analysis of the sample yielded Ca/P molar ratios in the range of 1.2-1.9, where the Ca/P molar ratio for the original glass coating was 7.7.

The layers morphologies and Ca/P molar ratios suggested the formation of HA precursors (after 3/7 day calcium deficient ACP, OCP). As the immersion time increased, well developed crystals were observed on the glass coating surfaces. The Ca/P molar ratios of layers formed on the surfaces evaluated with EDS analysis, gradually increased over immersion time from 1.38 for 3 days, trough 1.56 for 7 days, up to 1.63 for 14 days of immersion. The results indicate the HA layer formation on the glass coating surfaces occurred by progressively transformation of calcium phosphates [84]. Stanciu et al. [85] coated dental ceramics with a bioactive glass and showed through EDS analysis, that the Ca/P ratio between 9-th and 11-th days of immersion in SBF reached levels matching those of carbonate hydroxyapatite, which is 1.6 to 1.8.

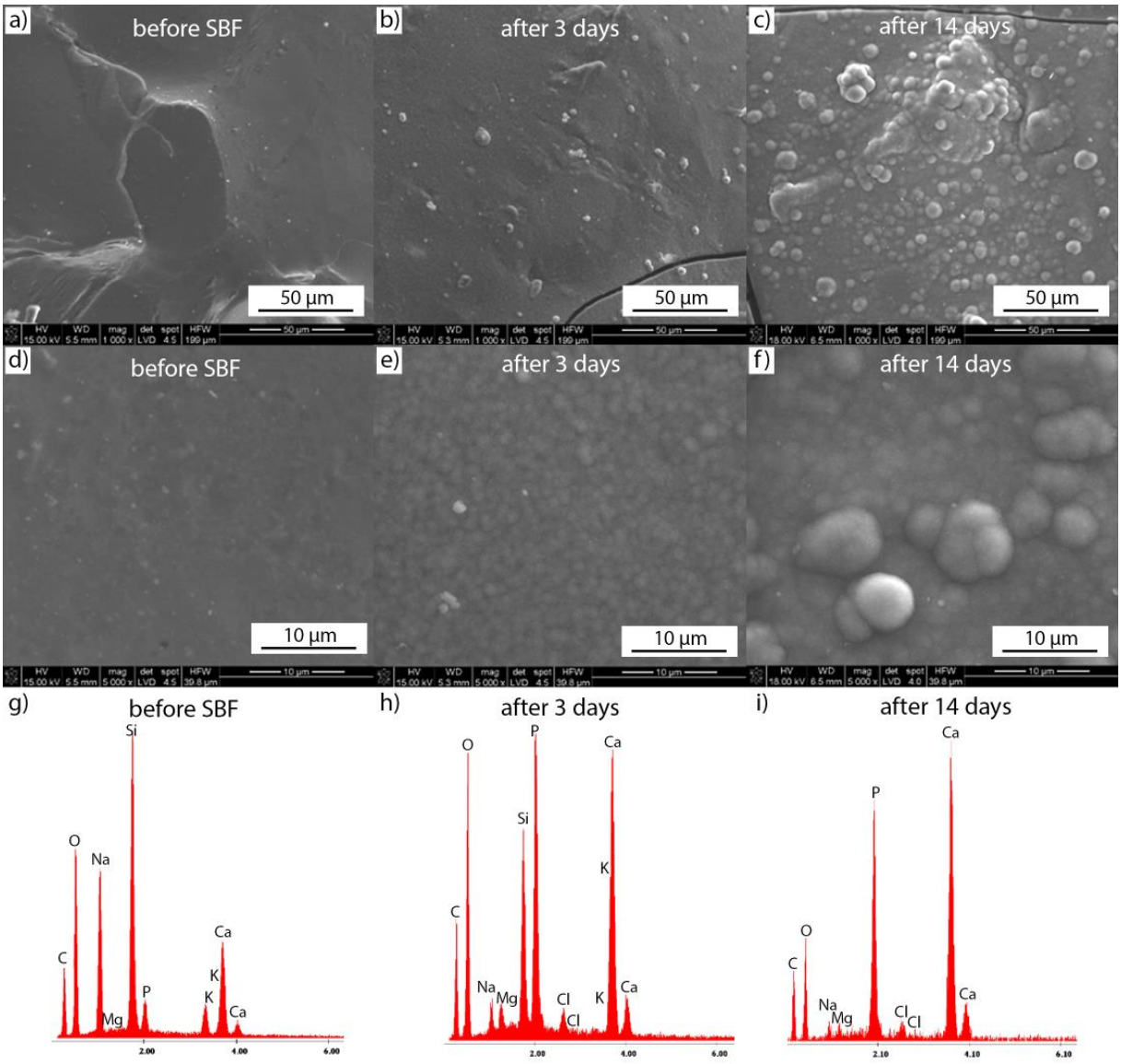

Fig. 15 a-f) SEM images of the bioactive glass coated onto the ultrafine-grained cpTi substrate before (a, d), after 3 (b, e) and after 14 (c, f) days of immersion in SBF, g-i) EDS spectrum of bioactive glass for the same time periods.

4.4 Numerical model validation

The model was validated in two ways. First, by comparing the calculated porosity level with the one achieved in the experiments. Second, by comparing the dimensions of melted zones obtained through numerical analysis and through experimental measurements. The numerical calculations showed that porosity level equals 16.2%, whereas the experimental one is about 15%. These values can be considered as comparable. Fig. 16 illustrates the temperature distribution in the metallic substrate during laser cladding of the bioactive glass track. The melting point of ultrafine-grained cpTi was assumed to be 1668°C and the grey colour indicates the areas at which the assumed melting temperature was exceeded. The grey region below the bioactive glass track indicates the melted zone. Its width and thickness are 330 and 50 µm, respectively. The obtained results are comparable with dimensions of the melted area identified using optical micrograph these were defined to be around 370 and 50 µm, respectively.

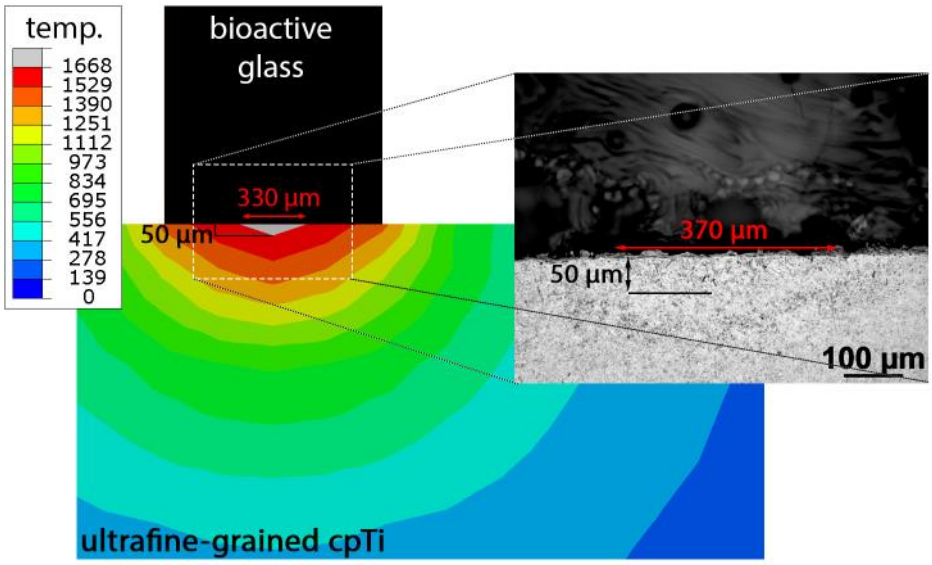

Fig. 16 Temperature distribution in ultrafine-grained cpTi substrate during the laser cladding process.

5. Conclusions

Laser cladding was used for the first time to obtain S520 bioactive glass coatings onto ultrafine-grained cpTi substrate. This approach allows for obtaining biomaterial, which is free from toxic elements and potentially applicable for load bearing biomedical implants. Several layers across the material cross section were identified through microscopic studies being characterised as melted zone and HAZ correspondingly. The formation of α' acicular martensite crystalline structure was found in the melted zone using SEM/EBSD analysis. HAZ and melted zones are characterized by relatively lower hardness, which indicates increased plastic properties of that part of the substrate. The martensitic microstructure gradually passes into relatively larger grains being approximately 10 µm in diameter. These grains are subsequently transformed into recrystallized smaller grains with a regular shape and diameter of about 2 µm. They are axisymmetric, and therefore free from disadvantages associated with anisotropy of mechanical properties. Such a combination of various zones with different properties may have synergistic effect and therefore is beneficial for the obtained biomaterials. EDS analysis showed that several glass elements are transferred to the substrate during the laser cladding. A characteristic region in the form of about 3 µm width band was formed in the melted zone about 10 µm below the titanium surface. Some amounts of Si, Na and P were found in the region while the titanium content in the same area was decreased. Such redistribution of the elements might be beneficial increasing adhesion between the bioactive glass coating and the substrate due to reduction of the CTE mismatch. The samples tested in vitro with SBF solution after 14 days revealed formation of spherical cauliflower-like forms typical to the morphology of HCA indicating high bioactivity of the bioactive glass coating.

Declaration of competing interest

The authors declare that they have no known competing financial interests or personal relationships that could have appeared to influence the work reported in this paper.

Acknowledgements

The support from the National Science Centre, Poland (grant no. DEC-2016/21/N/ST8/00091) is greatly appreciated. This research was supported in part by PLGrid Infrastructure.

Data availability

The data that support the findings of this study are available from the corresponding author upon reasonable request.

References

[1] M.S. Zafar, R. Ullah, Z. Qamar, M.A. Fareed, F. Amin, Z. Khurshid, F. Sefat, Properties of dental biomaterials, in: Adv. Dent. Biomater., Elsevier, 2019: pp. 7–35. https://doi.org/10.1016/b978-0-08-102476-8.00002-5.

[2] A. Sola, D. Bellucci, V. Cannillo, A. Cattini, Bioactive glass coatings: a review, Surf. Eng. 27 (2011) 560–572. https://doi.org/10.1179/1743294410Y.0000000008.

[3] A. Goharian, M.R. Abdullah, Bioinert Metals (Stainless Steel, Titanium, Cobalt Chromium), in: Trauma Plat. Syst., Elsevier, 2017: pp. 115–142. https://doi.org/10.1016/b978-0-12-804634-0.00007-0.

[4] S. Amin Yavari, J. van der Stok, Y.C. Chai, R. Wauthle, Z. Tahmasebi Birgani, P. Habibovic, M. Mulier, J. Schrooten, H. Weinans, A.A. Zadpoor, Bone regeneration performance of surface-treated porous titanium, Biomaterials. 35 (2014) 6172–6181. https://doi.org/10.1016/j.biomaterials.2014.04.054.

[5] N. Eliaz, Corrosion of Metallic Biomaterials: A Review, Materials (Basel). 12 (2019) 407. https://doi.org/10.3390/ma12030407.

[6] U.J. Schlegel, N.E. Bishop, K. Püschel, M.M. Morlock, K. Nagel, Comparison of different cement application techniques for tibial component fixation in TKA, Int. Orthop. (2014) 47–54. https://doi.org/10.1007/s00264-014-2468-x.

[7] W. Cao, L.L. Hench, Bioactive materials, Ceram. Int. 22 (1996) 493–507. https://doi.org/10.1016/0272-8842(95)00126-3.

[8] L.L. Hench, Biomaterials: A forecast for the future, Biomaterials. 19 (1998) 1419–1423. https://doi.org/10.1016/S0142-9612(98)00133-1.

[9] C. Aparicio, M.P. Ginebra, Biomineralization and Biomaterials, Elsevier, 2016. https://doi.org/10.1016/C2014-0-02825-0.

[10] L.L. Hench, H.A. Paschall, Direct chemical bond of bioactive glass-ceramic materials to bone and muscle., J. Biomed. Mater. Res. 7 (1973) 25–42. https://doi.org/10.1002/jbm.820070304.

[11] L.L. Hench, The story of Bioglass®, J. Mater. Sci. Mater. Med. 17 (2006) 967–978. https://doi.org/10.1007/s10856-006-0432-z.

[12] L.L. Hench, J. Wilson, An Introduction to Bioceramics, 1993. https://doi.org/10.1142/9781908977168_0021.

[13] H.R. Fernandes, A. Gaddam, A. Rebelo, D. Brazete, G.E. Stan, J.M.F. Ferreira, Bioactive Glasses and Glass-Ceramics for Healthcare Applications in Bone Regeneration and Tissue Engineering, Materials (Basel). 11 (2018) 2530. https://doi.org/10.3390/ma11122530.

[14] L.L. Hench, J.R. Jones, Biomaterials, artificial organs and tissue engineering, Woodhead Publishing Limited, 2005. https://doi.org/10.1533/9781845690861.

[15] B. Prabhu, A. Karau, A. Wood, M. Dadsetan, H. Liedtke, T. Dewitt, Bioresorbable materials for orthopedic applications (Lactide and glycolide based), in: Orthop. Biomater. Prog. Biol. Manuf. Ind. Perspect., Springer International Publishing, 2018: pp. 287–344. https://doi.org/10.1007/978-3-319-89542-0_13.

[16] M. Vallet-Regí, Evolution of bioceramics within the field of biomaterials, Comptes Rendus Chim. 13 (2010) 174–185. https://doi.org/10.1016/j.crci.2009.03.004.

[17] C. Arts, J. Geurts, Management of Periprosthetic Joint Infections (PJIs), Elsevier, 2017. http://linkinghub.elsevier.com/retrieve/pii/B9780081002056099894 (accessed October 31, 2019).
[18] V. Miguez-Pacheco, L.L. Hench, A.R. Boccaccini, Bioactive glasses beyond bone and teeth: Emerging applications in contact with soft tissues, Acta Biomater. 13 (2015) 1–15. https://doi.org/10.1016/j.actbio.2014.11.004.
[19] H. Ylänen, Bioactive Glasses: Materials, Properties and Applications, Elsevier, 2018. https://doi.org/10.1016/C2015-0-05462-4.
[20] M. Krzyzanowski, S. Bajda, Y. Liu, A. Triantaphyllou, W. Mark Rainforth, M. Glendenning, 3D analysis of thermal and stress evolution during laser cladding of bioactive glass coatings, J. Mech. Behav. Biomed. Mater. 59 (2016) 404–417. https://doi.org/10.1016/j.jmbbm.2016.02.023.
[21] X. Liu, P.K. Chu, C. Ding, Surface modification of titanium, titanium alloys, and related materials for biomedical applications, Mater. Sci. Eng. R Reports. 47 (2004) 49–121. https://doi.org/10.1016/J.MSER.2004.11.001.
[22] C.N. Elias, M.A. Meyers, R.Z. Valiev, S.N. Monteiro, Ultrafine grained titanium for biomedical applications: An overview of performance, J. Mater. Res. Technol. 2 (2013) 340–350. https://doi.org/10.1016/j.jmrt.2013.07.003.
[23] M. Kaur, K. Singh, Review on titanium and titanium based alloys as biomaterials for orthopaedic applications, Mater. Sci. Eng. C. 102 (2019) 844–862. https://doi.org/10.1016/j.msec.2019.04.064.
[24] Y.P. Dong, J.C. Tang, D.W. Wang, N. Wang, Z.D. He, J. Li, D.P. Zhao, M. Yan, Additive manufacturing of pure Ti with superior mechanical performance, low cost, and biocompatibility for potential replacement of Ti-6Al-4V, Mater. Des. (2020). https://doi.org/10.1016/j.matdes.2020.109142.
[25] V. V. Stolyarov, Y.T. Zhu, I. V. Alexandrov, T.C. Lowe, R.Z. Valiev, Grain refinement and properties of pure Ti processed by warm ECAP and cold rolling, Mater. Sci. Eng. A. 343 (2003) 43–50. https://doi.org/10.1016/S0921-5093(02)00366-0.
[26] S.M. Baek, M.H. Shin, J. Moon, H.S. Jung, S.A. Lee, W. Hwang, J.T. Yeom, S.K. Hahn, H.S. Kim, Superior pre-osteoblast cell response of etched ultrafine-grained titanium with a controlled crystallographic orientation, Sci. Rep. 7 (2017). https://doi.org/10.1038/srep44213.
[27] R.Z. Valiev, Y. Estrin, Z. Horita, T.G. Langdon, M.J. Zehetbauer, Y.T. Zhu, Fundamentals of Superior Properties in Bulk NanoSPD Materials, Mater. Res. Lett. 3831 (2015) 1–21. https://doi.org/10.1080/21663831.2015.1060543.
[28] A. Panigrahi, B. Sulkowski, T. Waitz, K. Ozaltin, W. Chrominski, A. Pukenas, J. Horky, M. Lewandowska, W. Skrotzki, M. Zehetbauer, Mechanical properties, structural and texture evolution of biocompatible Ti–45Nb alloy processed by severe plastic deformation, J. Mech. Behav. Biomed. Mater. (2016). https://doi.org/10.1016/j.jmbbm.2016.04.042.
[29] K.A. Prosolov, O.A. Belyavskaya, U. Muehle, Y.P. Sharkeev, Thin bioactive Zn substituted hydroxyapatite coating deposited on ultrafine-grained titanium substrate: Structure analysis, Front. Mater. 5 (2018) 1–8. https://doi.org/10.3389/fmats.2018.00003.
[30] D. Bellucci, A. Sola, A. Anesi, R. Salvatori, L. Chiarini, V. Cannillo, Bioactive glass/hydroxyapatite composites: Mechanical properties and biological evaluation, Mater. Sci. Eng. C. 51 (2015) 196–205. https://doi.org/10.1016/j.msec.2015.02.041.
[31] A. Sola, D. Bellucci, V. Cannillo, Enamelled coatings produced with low-alkaline bioactive glasses, Surf. Coatings Technol. 248 (2014) 1–8. https://doi.org/10.1016/j.surfcoat.2014.03.025.

[32] V. Cannillo, A. Sola, Different approaches to produce coatings with bioactive glasses: Enamelling vs plasma spraying, J. Eur. Ceram. Soc. 30 (2010) 2031–2039. https://doi.org/10.1016/j.jeurceramsoc.2010.04.021.
[33] I. Corni, M.P. Ryan, A.R. Boccaccini, Electrophoretic deposition: From traditional ceramics to nanotechnology, J. Eur. Ceram. Soc. 28 (2008) 1353–1367. https://doi.org/10.1016/j.jeurceramsoc.2007.12.011.
[34] L. Torrisi, R. Setola, Thermally assisted hydroxyapatite obtained by pulsed-laser deposition on titanium substrates, Thin Solid Films. 227 (1993) 32–36. https://doi.org/10.1016/0040-6090(93)90183-P.
[35] G. Socol, P. Torricelli, B. Bracci, M. Iliescu, F. Miroiu, A. Bigi, J. Werckmann, I.N. Mihailescu, Biocompatible nanocrystalline octacalcium phosphate thin films obtained by pulsed laser deposition, Biomaterials. 25 (2004) 2539–2545. https://doi.org/10.1016/j.biomaterials.2003.09.044.
[36] C. Berbecaru, H. V. Alexandru, A. Ianculescu, A. Popescu, G. Socol, F. Sima, I. Mihailescu, Bioglass thin films for biomimetic implants, Appl. Surf. Sci. 255 (2009) 5476–5479. https://doi.org/10.1016/j.apsusc.2008.08.020.
[37] H. Paydas, A. Mertens, R. Carrus, J. Lecomte-Beckers, J. Tchoufang Tchuindjang, Laser cladding as repair technology for Ti-6Al-4V alloy: Influence of building strategy on microstructure and hardness, Mater. Des. (2015). https://doi.org/10.1016/j.matdes.2015.07.035.
[38] R. Comesaña, F. Quintero, F. Lusquiños, M.J. Pascual, M. Boutinguiza, A. Durán, J. Pou, Laser cladding of bioactive glass coatings, Acta Biomater. 6 (2010) 953–961. https://doi.org/10.1016/j.actbio.2009.08.010.
[39] P. Kongsuwan, G. Brandal, Y. Lawrence Yao, Laser Induced Porosity and Crystallinity Modification of a Bioactive Glass Coating on Titanium Substrates, J. Manuf. Sci. Eng. 137 (2015) 031004. https://doi.org/10.1115/1.4029566.
[40] M. Roy, B. Vamsi Krishna, A. Bandyopadhyay, S. Bose, Laser processing of bioactive tricalcium phosphate coating on titanium for load-bearing implants, Acta Biomater. 4 (2008) 324–333. https://doi.org/10.1016/j.actbio.2007.09.008.
[41] F. Lusquiños, A. De Carlos, J. Pou, J.L. Arias, M. Boutinguiza, B. León, M. Pérez-Amor, F.C.M. Driessens, K. Hing, I. Gibson, S. Best, W. Bonfield, Calcium phosphate coatings obtained by Nd:YAG laser cladding: physicochemical and biologic properties., J. Biomed. Mater. Res. A. 64 (2003) 630–637. https://doi.org/10.1002/jbm.a.10440.
[42] D. Bellucci, V. Cannillo, A. Sola, Coefficient of thermal expansion of bioactive glasses: Available literature data and analytical equation estimates, Ceram. Int. 37 (2011) 2963–2972. https://doi.org/10.1016/j.ceramint.2011.05.048.
[43] Y.Z. Tian, Y. Bai, M.C. Chen, A. Shibata, D. Terada, N. Tsuji, Enhanced Strength and Ductility in an Ultrafine-Grained Fe-22Mn-0.6C Austenitic Steel Having Fully Recrystallized Structure, Metall. Mater. Trans. A Phys. Metall. Mater. Sci. 45 (2014) 5300–5304. https://doi.org/10.1007/s11661-014-2552-2.
[44] S. Lee, J.Y. Oh, S. Mukaeyama, S.-H. Sun, T. Nakano, Preparation of Titanium Alloy/Bioactive Glass Composite for Biomedical Applications via Selective Laser Melting, Mater. Trans. 60 (2019) 1779–1784. https://doi.org/10.2320/matertrans.ME201914.
[45] S. Pauly, L. Löber, R. Petters, M. Stoica, S. Scudino, U. Kühn, J. Eckert, Processing metallic glasses by selective laser melting, Mater. Today. 16 (2013) 37–41. https://doi.org/10.1016/j.mattod.2013.01.018.
[46] O. Peitl Filho, G.P. LaTorre, L.L. Hench, Effect of crystallization on apatite-layer formation of bioactive glass 45S5., J. Biomed. Mater. Res. 30 (1996) 509–14.

https://doi.org/10.1002/(SICI)1097-4636(199604)30:4<509::AID-JBM9>3.0.CO;2-T.
[47] I. Izquierdo-Barba, M. Vallet-Regi, Mesoporous bioactive glasses: Relevance of their porous structure compared to that of classical bioglasses, Biomed. Glas. 1 (2015) 140–150. https://doi.org/10.1515/bglass-2015-0014.
[48] T. Amine, J.W. Newkirk, F. Liou, An investigation of the effect of direct metal deposition parameters on the characteristics of the deposited layers, Case Stud. Therm. Eng. 3 (2014) 21–34. https://doi.org/10.1016/j.csite.2014.02.002.
[49] I. V. Smirnov, Strength Characteristics and Fracture of Ultrafine-Grained Titanium Grade 4 Processed by Equal Channel Angular Pressing—Conform, Tech. Phys. 64 (2019) 497–505. https://doi.org/10.1134/S1063784219040212.
[50] S. Grasso, R.K. Chinnam, H. Porwal, A.R. Boccaccini, M.J. Reece, Low temperature spark plasma sintering of 45S5 Bioglass®, J. Non. Cryst. Solids. 362 (2013) 25–29. https://doi.org/10.1016/j.jnoncrysol.2012.11.009.
[51] J. Yang, S. Sun, M. Brandt, W. Yan, Experimental investigation and 3D finite element prediction of the heat affected zone during laser assisted machining of Ti6Al4V alloy, J. Mater. Process. Technol. 210 (2010) 2215–2222. https://doi.org/10.1016/j.jmatprotec.2010.08.007.
[52] N. Zotov, Heat capacity of sodium silicate glasses: comparison of experiments with computer simulations, J. Phys. Condens. Matter. 14 (2002) 11655–11669. https://doi.org/10.1088/0953-8984/14/45/309.
[53] G. Chassaing, A. Pougis, S. Philippon, P. Lipinski, J. Meriaux, Experimental and numerical study of frictional heating during rapid interactions of a Ti6Al4V tribopair, Wear. 342–343 (2015) 322–333. https://doi.org/10.1016/j.wear.2015.09.013.
[54] H. Koizumi, Y. Takeuchi, H. Imai, T. Kawai, T. Yoneyama, Application of titanium and titanium alloys to fixed dental prostheses, J. Prosthodont. Res. (2019). https://doi.org/10.1016/j.jpor.2019.04.011.
[55] S. Bajda, M. Krzyzanowski, Modelling Aspects Of Laser Cladding Of Bioactive Glass Coatings On Ultrafine-grained Titanium, Comput. Methods Mater. Sci. 19 (2019) 138–149.
[56] L. Pilon, F. Janos, R. Kitamura, Effective thermal conductivity of soda-lime silicate glassmelts with different iron contents between 1100°C and 1500°C, J. Am. Ceram. Soc. 97 (2014) 442–450. https://doi.org/10.1111/jace.12768.
[57] P. Coppa, A. Consorti, Normal emissivity of samples surrounded by surfaces at diverse temperatures, Measurement. 38 (2005) 124–131. https://doi.org/10.1016/j.measurement.2005.05.001.
[58] M. Avrami, Kinetics of phase change. I: General theory, J. Chem. Phys. 7 (1939) 1103–1112. https://doi.org/10.1063/1.1750380.
[59] W.A. Johnson, R.F. Mehl, Reaction Kinetics in Processes of Nucleation and Growth, Trans. Am. Inst. Min. Metall. Eng. 135 (1939) 416–442.
[60] A.N. Kolmogorov, On the Statistical Theory of Crystallization of Metals, Izv. Akad. Nauk SSSR. 3 (1937) 355–359.
[61] P. Krüger, On the relation between non-isothermal and isothermal Kolmogorov-Johnson-Mehl-Avrami crystallization kinetics, J. Phys. Chem. Solids. 54 (1993) 1549–1555. https://doi.org/10.1016/0022-3697(93)90349-V.
[62] L. Lefebvre, J. Chevalier, L. Gremillard, R. Zenati, G. Thollet, D. Bernache-Assolant, A. Govin, Structural transformations of bioactive glass 45S5 with thermal treatments, Acta Mater. 55 (2007) 3305–3313. https://doi.org/10.1016/j.actamat.2007.01.029.
[63] A.R. Boccaccini, Q. Chen, L. Lefebvre, L. Gremillard, J. Chevalier, Sintering, crystallisation and biodegradation behaviour of Bioglass®-derived glass-ceramics,

Faraday Discuss. 136 (2007) 27–44. https://doi.org/10.1039/b616539g.
[64] S. Kolossov, E. Boillat, R. Glardon, P. Fischer, M. Locher, 3D FE simulation for temperature evolution in the selective laser sintering process, Int. J. Mach. Tools Manuf. 44 (2004) 117–123. https://doi.org/10.1016/j.ijmachtools.2003.10.019.
[65] J. Frenkel, Viscous flow of crystalline bodies under the action of surface tension, J. Phys. 9 (1945) 385–391. https://doi.org/10.4319/lo.2013.58.2.0489.
[66] J.M. Park, D.S. Kim, S.R. Kim, Interfacial properties and microfailure degradation mechanisms of bioabsorbable fibers/poly-L-lactide composites using micromechanical test and nondestructive acoustic emission, Compos. Sci. Technol. 63 (2003) 403–419. https://doi.org/10.1016/S0266-3538(02)00212-9.
[67] M.A. Bouhifd, P. Richet, P. Besson, M. Roskosz, J. Ingrin, Redox state, microstructure and viscosity of a partially crystallized basalt melt, Earth Planet. Sci. Lett. 218 (2004) 31–44. https://doi.org/10.1016/S0012-821X(03)00641-1.
[68] P. Kongsuwan, Laser Induced Modification and Integration of Glasses, 2014.
[69] T.K. Gupta, R.L. Coble, Sintering of ZnO: II, Density Decrease and Pore Growth During the Final Stage of the Process, J. Am. Ceram. Soc. 51 (1968) 525–528. https://doi.org/10.1111/j.1151-2916.1968.tb15680.x.
[70] I. Smirnov, A. Polyakov, Y. Sudenkov, Strength and fracture of ultrafine-grained titanium Grade 4, Procedia Struct. Integr. 6 (2017) 196–200. https://doi.org/10.1016/j.prostr.2017.11.030.
[71] A. V. Polyakov, I.P. Semenova, G.I. Raab, V.D. Sitdikov, R.Z. Valiev, Peculiarities of ultrafine-grained structure formation in Ti grade-4 using ECAP-Conform, Rev. Adv. Mater. Sci. 31 (2012) 78–84.
[72] I. Sabirov, M.T. Perez-Prado, J.M. Molina-Aldareguia, I.P. Semenova, G.K. Salimgareeva, R.Z. Valiev, Anisotropy of mechanical properties in high-strength ultra-fine-grained pure Ti processed via a complex severe plastic deformation route, Scr. Mater. 64 (2011) 69–72. https://doi.org/10.1016/j.scriptamat.2010.09.006.
[73] B. Huang, Y. Zhai, S. Liu, X. Mao, Microstructure anisotropy and its effect on mechanical properties of reduced activation ferritic/martensitic steel fabricated by selective laser melting, J. Nucl. Mater. 500 (2018) 33–41. https://doi.org/10.1016/j.jnucmat.2017.12.011.
[74] T. Kokubo, H. Takadama, How useful is SBF in predicting in vivo bone bioactivity?, Biomaterials. (2006). https://doi.org/10.1016/j.biomaterials.2006.01.017.
[75] Z. Sun, I. Annergren, D. Pan, T.A. Mai, Effect of laser surface remelting on the corrosion behavior of commercially pure titanium sheet, Mater. Sci. Eng. A. 345 (2003) 293–300. https://doi.org/10.1016/S0921-5093(02)00477-X.
[76] J. He, D. Li, W. Jiang, L. Ke, G. Qin, Y. Ye, Q. Qin, D. Qiu, The Martensitic Transformation and Mechanical Properties of Ti6Al4V Prepared via Selective Laser Melting, Materials (Basel). 12 (2019) 321. https://doi.org/10.3390/ma12020321.
[77] P. Kuo, S.S. Joshi, X. Lu, Y. Ho, Y. Xiang, N.B. Dahotre, J. Du, Laser coating of bioactive glasses on bioimplant titanium alloys, Int. J. Appl. Glas. Sci. 10 (2019) 307–320. https://doi.org/10.1111/ijag.12642.
[78] E. Verné, M. Ferraris, A. Ventrella, L. Paracchini, A. Krajewski, A. Ravaglioli, Sintering and plasma spray deposition of bioactive glass-Matrix composites for medical applications, J. Eur. Ceram. Soc. 18 (1998) 363–372. https://doi.org/10.1016/S0955-2219(97)00134-9.
[79] J. Del Val, R. López-Cancelos, A. Riveiro, A. Badaoui, F. Lusquiños, F. Quintero, R. Comesaña, M. Boutinguiza, J. Pou, On the fabrication of bioactive glass implants for bone regeneration by laser assisted rapid prototyping based on laser cladding, Ceram. Int. 42 (2016) 2021–2035. https://doi.org/10.1016/j.ceramint.2015.10.009.

[80] R. Comesaña, F. Lusquiños, J. Del Val, M. López-Álvarez, F. Quintero, A. Riveiro, M. Boutinguiza, A. De Carlos, J.R. Jones, R.G. Hill, J. Pou, Three-dimensional bioactive glass implants fabricated by rapid prototyping based on CO2laser cladding, Acta Biomater. 7 (2011) 3476–3487. https://doi.org/10.1016/j.actbio.2011.05.023.
[81] O. Peitl, E. Dutra Zanotto, L.L. Hench, Highly bioactive P2O5-Na2O-CaO-SiO2glass-ceramics, J. Non. Cryst. Solids. 292 (2001) 115–126. https://doi.org/10.1016/S0022-3093(01)00822-5.
[82] L. Moimas, G. De Rosa, V. Sergo, C. Schmid, Bioactive porous scaffolds for tissue engineering applications: investigation on the degradation process by Raman spectroscopy and scanning electron microscopy., J. Appl. Biomater. Biomech. 4 (2006) 102–109. http://www.ncbi.nlm.nih.gov/pubmed/20799209 (accessed February 5, 2021).
[83] L. Peddi, R.K. Brow, R.F. Brown, Bioactive borate glass coatings for titanium alloys, J. Mater. Sci. Mater. Med. 19 (2008) 3145–3152. https://doi.org/10.1007/s10856-008-3419-0.
[84] M. Dziadek, B. Zagrajczuk, E. Menaszek, K. Dziadek, K. Cholewa-Kowalska, Poly(ε-caprolactone)-based membranes with tunable physicochemical, bioactive and osteoinductive properties, J. Mater. Sci. 52 (2017) 12960–12980. https://doi.org/10.1007/s10853-017-1424-8.
[85] G. Stanciu, I. Sandulescu, B. Savu, Investigation of the Hydroxyapatite Growth on Bioactive Glass Surface, J. Biomed. & 1 (2007) 34–39. http://www3.ntu.edu.sg/bmerc/contents/JBPE/J001/JBPE 1(1); 34-39.pdf.